Journal of Computational Physics 419 (2020) 109685

Contents lists available at ScienceDirect

Journal of Computational Physics

www.elsevier.com/locate/jcp

A space-time discontinuous Galerkin method for the elastic wave equation

Paola F. Antonietti, Ilario Mazzieri, Francesco Migliorini *

MOX, Laboratory for Modeling and Scientific Computing, Dipartimento di Matematica, Politecnico di Milano, Piazza Leonardo da Vinci 32, I-20133 Milano, Italy

ARTICLE INFO

Article history:
Received 25 October 2019
Received in revised form 21 May 2020
Accepted 15 June 2020
Available online 29 June 2020

Keywords:
Discontinuous Galerkin methods
Wave equation
Space-time finite elements
Stability and convergence analysis

ABSTRACT

In this work we present a new high order space-time discretization method based on a discontinuous Galerkin paradigm for the second order visco-elastodynamics equation. After introducing the method, we show that the resulting space-time discontinuous Galerkin formulation is well-posed, stable and retains optimal rate of convergence with respect to the discretization parameters, namely the mesh size and the polynomial approximation degree. A set of two and three-dimensional numerical experiments confirms the theoretical bounds.

1. Introduction

Hyperbolic initial-boundary value problems, such as wave propagation phenomena, arise in many and different engineering disciplines: in sound and vibration analysis, in medical imaging, in sonar or radar detection, in computational seismology and in life and social sciences. Developing numerical methods for this class of problems has been a constant interest in the field of computational mechanics and engineering. To represent effectively the underlying physical phenomenon it is needed: i) an accurate representation of the waves propagating through the elastic or acoustic medium, ii) a detailed description of the involved geometry (such as complex surfaces and irregular interfaces) and iii) a considerable amount of computational effort in order to resolve the problem for all the wavelenghts of interest.

Standard discretization methods in time and space are based on time-stepping methods (e.g. finite differences, Newmark or Runge-Kutta type schemes) combined with suitable spatial discretization techniques, like finite element methods. In this framework we can distinguish two families of methods: i) the method of lines, cf. [40] (first discretize in space and then solve the resulting ordinary differential equation) and ii) the Rothe method (first discretize in time and then solve the resulting partial differential equation), cf. [39].

More recently, discretizations of hyperbolic equations consider the full problem in the space-time configuration, i.e. the finite element method is also used to discretize the temporal domain, and aim to overcome limitations of classical approaches such as issues of stability and convergence with the choice of parameters. Space-time finite element schemes can be divided in two classes according to which type of mesh they employ, i.e., an unstructured simplicial or a structured prismatic grid.

* Corresponding author.
E-mail addresses: paola.antonietti@polimi.it (P.F. Antonietti), ilario.mazzieri@polimi.it (I. Mazzieri), francesco.migliorini@polimi.it (F. Migliorini).

https://doi.org/10.1016/j.jcp.2020.109685
0021-9991/

The first approach allows for discretization in time and space simultaneously because the temporal domain is treated as an additional dimension and a $d+1$-dimensional partition can be constructed directly in the space-time domain. In this sense, a one dimensional evolution problem is hence treated as a two dimensional one by considering, for instance, a triangular mesh. On the one hand, this approach has become quite popular and has been widely employed for problems that require deforming and/or moving meshes. In this context, the "tent pitching" algorithm [26] is used to build a simplicial space-time mesh upon which different approximation strategies can be employed, cf. [31,49] and references therein. See also [34,14,16,37]. On the other hand, although recent advances in the generation of unstructured simplicial space-time meshes, see [62,25], its construction for realistic three dimensional problems, hence composed of fourth dimensional polytopes, is still problematic and not easily achievable. It is mainly for that reason that space-time structured meshes are still preferable for three dimensional applications. Indeed, these grids can be easily obtained by extruding, in the time direction, the (generally) unstructured spatial mesh, giving rise to prismatic elements. The approximations built on top of such grids is less flexible that the one made by generic polytopes, but still allows for adaptivity. Additionally, the construction of space-time finite elements is very natural in this setting, [18,58,15].

Looking only at time discretization, we can distinguish between time continuous space-time Galerkin method (TcG) and time-discontinuous Galerkin method (TdG). In TcG schemes no discontinuity in time is allowed in the approximation. In its general implementation, TcG involves high computational cost because the entire temporal domain has to be discretized. Relevant applications to the wave propagation problem can be found in [1,63,32,42,29,41]. We refer the reader to [35,36] for an exhaustive review on the subject.

In TdG schemes the time interval is further subdivided into independent time slabs and temporal discontinuities or jumps are allowed between the slabs. The finite element approach is applied in each time slab and the unknowns that are solved in one time slab serve as inputs for the following one. This formulation is much more efficient than the TcG one for obvious reasons. In particular, it has been shown that TdG scheme leads to approximations that are A-stable and high order accurate. In literature, it is possible to find different TdG finite element formulations that are built upon reformulating the original problem as a system of first-order equations (see, e.g., [22,34,38,28]) or directly applied to the second-order hyperbolic system, where a Galerkin least square (GLS) approach is applied to stabilize the numerical scheme, e.g., [36,59,4,64]).

Finally, in the framework of high order space-time methods for hyperbolic equations, we also mention a family of techniques based on the resolution of the Generalized Riemann Problem (GRP) [60], namely the ADER (Arbitrary high order using DERivative) method, [61] and its variants, for example [24,45], where a finite volume discontinuous Galerkin approach is employed, cf. also [23,27,55,56].

In this paper we develop a new high-order *space-time* dG finite element method for the resolution of the visco-elastodynamics equation on prismatic grids. The scheme that we propose is the result of a combination between the *space* dG formulation introduced in [13] and the *time* dG approximation presented in [8]. In particular, for the spatial discretization is employed a combined dG-cG approach where the solution is allowed to be discontinuous subdomain-wise while it is continuous inside each subdomain and approximated with spectral elements, see e.g., [10,46,11]. For the time integration a recently introduced TdG method is applied to the second-order differential problem, [8] stemming after space discretization. The obtained TdG method is implicit and unconditionally stable, allowing independent displacement interpolations between different time slabs. This new space-time method is naturally suited for an adaptive choice of the time discretization parameters, i.e., the use of high-order polynomials/small time steps only when the solution features a sharp spatial-temporal derivative.

The remainder of the paper is organized as follows. In Section 2 we formulate the problem, we describe separately the space and time discretization techniques and their main properties. Then, we present the space-time dG method and we analyze its well-posedness. In Section 3 we derive the algebraic formulation while in Section 4 we investigate the stability of the scheme and we prove an *a-priori* error estimates. Finally, numerical results are shown in Section 5 concerning the verification and the validation of the proposed discretization. Throughout the paper, we use standard notation for Sobolev spaces [3]. The Sobolev spaces of vector–valued and symmetric tensor-valued functions are denoted by $\mathbf{H}^m(D)=[H^m(D)]^d$ and $\boldsymbol{\mathcal{H}}^m(D)=[H^m(D)]^{d\times d}_{\rm sym}$, respectively. We will use the symbol $(\cdot,\cdot)_D$ to denote the standard inner product in any of the spaces $\mathbf{H}^0(D)=\mathbf{L}^2(D)$ or $\boldsymbol{\mathcal{H}}^0(D)=\boldsymbol{\mathcal{L}}^2(D)$. For time dependent functions we define, for any $T>0$, the spaces

$$L^q(0,T;H^s(\Omega))=\{w:(0,T)\to H^s(\Omega):\int_0^T ||w||^q_{H^s(\Omega)}\mathrm{d}t<+\infty,\quad 1\le q<\infty\},$$

and

$$H^q(0,T;H^s(\Omega))=\{w:(0,T)\to H^s(\Omega):\int_0^T ||w^{(k)}||^2_{H^s(\Omega)}\mathrm{d}t<+\infty,\ 1\le q<\infty,\ 0\le k\le q\},$$

for any $0\le s<\infty$. We define analogously the spaces $C^q(0,T;H^s(\Omega))$ for any $0\le q\le\infty, 0\le s<\infty$ as well as the corresponding vector-valued counterparts. In the following C denotes a generic positive constant that may take different values in different places, but is always mesh (either in space and time) independent. The notation $x\lesssim y$ will represent the inequality $x\le Cy$ for a constant C as before.

2. The visco-elastic wave propagation problem

We consider the general visco-elastic wave propagation problem in an open bounded polygonal domain $\Omega \subset \mathbb{R}^d$, $d = 2, 3$, with boundary $\partial\Omega = \Gamma_D \cup \Gamma_N$ such that $\Gamma_D \cap \Gamma_N = \emptyset$, and $|\Gamma_D| > 0$. The problem reads as follows: for $T > 0$ find $\boldsymbol{u} : \Omega \times (0, T] \to \mathbb{R}^d$ such that

$$\begin{cases} \rho \partial_{tt} \boldsymbol{u} + 2\rho\zeta \partial_t \boldsymbol{u} + \rho\zeta^2 \boldsymbol{u} - \nabla \cdot \boldsymbol{\sigma}(\boldsymbol{u}) = \boldsymbol{f}, & \text{in } \Omega \times (0, T], \\ \boldsymbol{\sigma}(\boldsymbol{u}) - \boldsymbol{D}\boldsymbol{\epsilon}(\boldsymbol{u}) = \boldsymbol{0}, & \text{in } \Omega \times (0, T], \\ \boldsymbol{u} = \boldsymbol{0}, & \text{on } \Gamma_D \times (0, T], \\ \boldsymbol{\sigma}(\boldsymbol{u})\boldsymbol{n} = \boldsymbol{0}, & \text{on } \Gamma_N \times (0, T], \\ \partial_t \boldsymbol{u}(0) = \hat{\boldsymbol{u}}_1(\boldsymbol{x}), & \text{in } \Omega \times \{0\}, \\ \boldsymbol{u}(0) = \hat{\boldsymbol{u}}_0(\boldsymbol{x}), & \text{in } \Omega \times \{0\}, \end{cases} \tag{1}$$

where $\rho \in L^\infty(\Omega)$ is a positive, bounded function representing the mass density of the medium, $\zeta \in L^\infty(\Omega)$ is a positive decay factor whose dimension is the inverse of time, $\boldsymbol{f} \in C^1((0, T]; \boldsymbol{L}^2(\Omega))$ is a given source term, $\hat{\mathbf{u}}_0 \in \mathbf{H}^1_{0,\Gamma_D}(\Omega) \cap \mathbf{H}^\Delta_{\boldsymbol{D}}(\Omega)$ and $\hat{\mathbf{u}}_1 \in \mathbf{H}^1_{0,\Gamma_D}(\Omega)$ are smooth enough initial conditions and

$$\mathbf{H}^1_{0,\Gamma_D}(\Omega) = \{\boldsymbol{w} \in \mathbf{H}^1(\Omega) : \boldsymbol{w} = \boldsymbol{0} \text{ on } \Gamma_D\},$$
$$\mathbf{H}^\Delta_{\boldsymbol{D}}(\Omega) = \{\boldsymbol{w} \in \mathbf{L}^2(\Omega) : \mathrm{div}(\boldsymbol{D}\boldsymbol{\epsilon}(\boldsymbol{w})) \in \mathbf{L}^2(\Omega)\}.$$

We remark that the damping factor ζ has been introduced to model viscoelastic effects without resorting to constitutive laws based on Prony series, which involve time convolutions to express the stress in terms of the strain history (see e.g. [50,51]). The main idea is to regard the sum of ζ-dependent terms as a viscous displacement-dependent volume force $\boldsymbol{f}_{vs} = -2\rho\zeta\partial_t\boldsymbol{u} - \rho\zeta^2\boldsymbol{u}$ acting upon a purely elastic body undergoing a displacement field $\boldsymbol{u}$ (see e.g. [10]). It can be shown that, considering an harmonic excitation, the solution $\boldsymbol{u}$ obtained by adding the viscous force can be related to the solution $\hat{\boldsymbol{u}}$ of the corresponding linear elastic problem by the relation $\boldsymbol{u} = e^{-\zeta t}\hat{\boldsymbol{u}}$. Hence, every frequency component of the solution to the linear elastic problem is attenuated by an exponential factor.

The second equation in (1) is the Hooke's constitutive law and relates the strain tensor $\boldsymbol{\epsilon}(\boldsymbol{u}) = \frac{1}{2}(\nabla\boldsymbol{u} + \nabla\boldsymbol{u}^T)$ to the stress tensor $\boldsymbol{\sigma}$ through the 4th order uniformly bounded symmetric and positive definite stiffness tensor $\boldsymbol{D}$ defined as follows

$$\boldsymbol{D}\boldsymbol{\epsilon} = 2\mu\boldsymbol{\epsilon} + \lambda\mathrm{tr}(\boldsymbol{\epsilon})\boldsymbol{I}. \tag{2}$$

In (2), λ and μ are the first and second Lamé elastic coefficients, respectively, while $\mathrm{tr}(\cdot)$ is the trace operator and $\boldsymbol{I} \in \mathbb{R}^{d\times d}$ is the identity tensor. Hereafter, we suppose that λ and μ are uniformly bounded positive functions in Ω, i.e., $\lambda, \mu \in L^\infty(\Omega)$, $\lambda, \mu > 0$. Next, we consider the variational formulation of problem (1): for all $t \in (0, T]$ find $\mathbf{u} \in \mathbf{H}^1_{0,\Gamma_D}(\Omega)$ such that:

$$(\rho\boldsymbol{u}_{tt}, \mathbf{v})_\Omega + (2\rho\zeta\partial_t\boldsymbol{u}, \mathbf{v})_\Omega + (\rho\zeta^2\boldsymbol{u}, \mathbf{v})_\Omega + (\boldsymbol{\sigma}(\boldsymbol{u}), \boldsymbol{\epsilon}(\mathbf{v}))_\Omega = (\boldsymbol{f}, \mathbf{v})_\Omega \qquad \forall \mathbf{v} \in \mathbf{H}^1_{0,\Gamma_D}(\Omega), \tag{3}$$

supplemented with the initial conditions $\mathbf{u}(0) = \hat{\mathbf{u}}_0$ and $\mathbf{u}_t 0 = \hat{\mathbf{u}}_1$. Under the above regularity assumptions problem (3) has a unique solution $\mathbf{u} \in C^2(0, T; \mathbf{L}^2(\Omega)) \cap C^1(0, T; \mathbf{H}^1_{0,\Gamma_D}(\Omega)) \cap C^0(0, T; \mathbf{H}^1_{0,\Gamma_D}(\Omega) \cap \mathbf{H}^\Delta_{\boldsymbol{D}}(\Omega))$, see for instance [6, Theorem 3.1].

2.1. Space discretization based on a dG spectral element method

We consider a (not necessarily conforming) decomposition $\mathcal{T}_h$ of Ω into L non-overlapping polyhedral sub-domains Ω_ℓ, i.e., $\overline{\Omega} = \cup_\ell \overline{\Omega}_\ell$, $\Omega_\ell \cap \Omega_{\ell'} = \emptyset$ for $\ell \neq \ell'$. On each Ω_ℓ, we build a *conforming*, *quasi-uniform* computational mesh $\mathcal{T}_{h_\ell}$ of granularity $h_\ell > 0$ made by open disjoint elements $\mathcal{K}^j_\ell$, and suppose that each $\mathcal{K}^j_\ell \in \Omega_\ell$ is the affine image through the map $F^j_\ell : \widehat{\mathcal{K}} \longrightarrow \mathcal{K}^j_\ell$ of either the unit reference hexahedron (resp. square) or the unit reference tetrahedron (resp. triangle) $\widehat{\mathcal{K}}$ for $d = 3$ (resp. $d = 2$), see Fig. 1. Given two adjacent regions $\Omega_{\ell^\pm}$, we define an interior face F as the non-empty interior of $\partial\overline{\mathcal{K}^+} \cap \partial\overline{\mathcal{K}^-}$, for some $\mathcal{K}^\pm \in \mathcal{T}_{h_{\ell^\pm}}$, $\mathcal{K}^\pm \subset \Omega_{\ell^\pm}$, and collect all the interior faces in the set $\mathcal{F}^I_h$. Moreover, we define $\mathcal{F}^D_h$ and $\mathcal{F}^N_h$ as the sets of all boundary faces where displacement and traction are imposed, respectively. Implicit in this definition is the assumption that each boundary face can belong to exactly one of the sets $\mathcal{F}^D_h$ or $\mathcal{F}^N_h$. Finally, we collect all the boundary faces in the set $\mathcal{F}^b_h$. To carry out the analysis, we suppose that the following shape-regularity mesh assumption holds, see [48,30].

Assumption 2.1. Mesh assumption. For any element $K \in \mathcal{T}_h$ and for any face $F \subset \partial K$, it holds $h_K \lesssim h_F$.

Assumption 2.2. Local bounded variation. Mesh-size h_ℓ and polynomial degree N_ℓ have local bounded variation, i.e. $h_{\ell^+} \lesssim h_{\ell^-} \lesssim h_{\ell^+}$ and $N_{\ell^+} \lesssim N_{\ell^-} \lesssim N_{\ell^+}$ for any pair of neighboring elements $\Omega_{\ell^\pm}$.

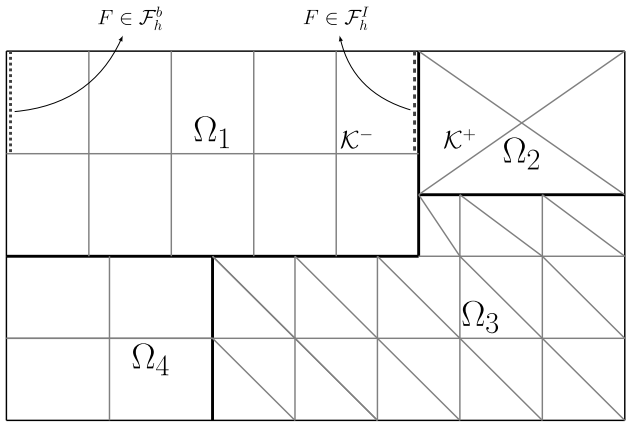

Fig. 1. Two dimensional example of the domain decomposition partition. Non-conforming subdomain partition $\overline{\Omega} = \cup_\ell \overline{\Omega}_\ell$ and conforming quasi-uniform computational mesh within each Ω_ℓ.

We refer to [19], for example, for the weakening of the above assumptions and to [18,7,12] for the use of polyhedral-shaped elements.

Let $\mathcal{K}^\pm \in \mathcal{T}_{h_{\ell^\pm}}$ be two elements sharing a face $F \in \mathcal{F}_h^I$, and let $\boldsymbol{n}^\pm$ be the unit normal vectors to F pointing outward to $\mathcal{K}^\pm$, respectively. For (regular enough) vector and tensor-valued functions $\mathbf{w}$ and $\boldsymbol{\tau}$, respectively, we denote by $\mathbf{w}^\pm$ and $\boldsymbol{\tau}^\pm$ the traces of $\mathbf{w}$ and $\boldsymbol{\tau}$ on F, taken within the interior of $\mathcal{K}^\pm$, respectively, and set

$$[\![\boldsymbol{w}]\!] = \boldsymbol{w}^+ \odot \boldsymbol{n}^+ + \boldsymbol{w}^- \odot \boldsymbol{n}^-, \quad [\![\boldsymbol{\tau}]\!] = \boldsymbol{\tau}^+ \boldsymbol{n}^+ + \boldsymbol{\tau}^- \boldsymbol{n}^-, \quad \{\boldsymbol{w}\} = \frac{\boldsymbol{w}^+ + \boldsymbol{w}^-}{2}, \quad \{\boldsymbol{\tau}\} = \frac{\boldsymbol{\tau}^+ + \boldsymbol{\tau}^-}{2},$$

where $\boldsymbol{w} \odot \boldsymbol{n} = (\boldsymbol{w}^T \boldsymbol{n} + \boldsymbol{n}^T \boldsymbol{w})/2$.

Now, to each subdomain Ω_ℓ we assign a nonnegative integer N_ℓ, and introduce the finite dimensional spaces for $\ell = 1, \ldots, L$,

$$\mathbf{V}_{h^\ell}^{N_\ell}(\Omega^\ell) = \{\boldsymbol{w} \in \mathbf{C}^0(\overline{\Omega}_\ell) : \boldsymbol{w}|_{\mathcal{K}_\ell^j} \circ F_\ell^j \in [\mathbb{M}^{N_\ell}(\widehat{\mathcal{K}})]^d \quad \forall\, \mathcal{K}_\ell^j \in \mathcal{T}_{h_\ell},\ \boldsymbol{w} = \mathbf{0} \text{ on } \Gamma_D\}, \tag{4}$$

where $\mathbb{M}^{N_k}(\widehat{\mathcal{K}})$ is either the space $\mathbb{P}^{N_k}(\widehat{\mathcal{K}})$ of polynomials of total degree at most N_k on $\widehat{\mathcal{K}}$, if $\widehat{\mathcal{K}}$ is the reference tetrahedron (resp. triangle), or the space $\mathbb{Q}^{N_k}(\widehat{\mathcal{K}})$ of polynomials of degree N_k in each coordinate direction on $\widehat{\mathcal{K}}$, if $\widehat{\mathcal{K}}$ is the unit reference hexahedron (resp. square) in $\mathbb{R}^3$ (resp. $\mathbb{R}^2$). We then define the space $\boldsymbol{V}_h^N$ as $\boldsymbol{V}_h^N = \prod_\ell \mathbf{V}_{h^\ell}^{N_\ell}(\Omega^\ell)$. The semi-discrete dG spectral element approximation of problem (3) reads: $\forall t \in (0, T]$, find $\boldsymbol{u}_h = \boldsymbol{u}_h(t) \in \boldsymbol{V}_h^N$ such that

$$\sum_{\ell=1}^{L} \Big[(\rho \ddot{\boldsymbol{u}}_h, \boldsymbol{v})_{\Omega_\ell} + (2\rho\zeta \dot{\boldsymbol{u}}_h, \boldsymbol{v})_{\Omega_\ell} + (\rho\zeta^2 \boldsymbol{u}_h, \boldsymbol{v})_{\Omega_\ell} \Big] + \mathcal{B}_h(\boldsymbol{u}_h, \boldsymbol{v}) = \mathcal{F}_h(\boldsymbol{v}) \quad \forall\, \boldsymbol{v} \in \boldsymbol{V}_h^N, \tag{5}$$

subjected to the initial conditions $\mathbf{u}_h(0) = \hat{\mathbf{u}}_{0,h}$ and $\dot{\mathbf{u}}(0) = \hat{\mathbf{u}}_{1,h}$, where $\hat{\mathbf{u}}_{0,h}$ and $\hat{\mathbf{u}}_{1,h}$ are suitable approximation to $\hat{\mathbf{u}}_0$ and $\hat{\mathbf{u}}_1$, respectively. In (5) the right-hand side $\mathcal{F}_h(\cdot)$ is defined as

$$\mathcal{F}_h(\boldsymbol{v}) = \sum_{\ell=1}^{L} (\mathbf{f}, \boldsymbol{v})_{\Omega_\ell} \qquad \boldsymbol{v} \in \boldsymbol{V}_h^N, \tag{6}$$

while the bilinear form $\mathcal{B}_h(\cdot, \cdot)$ is given by

$$\mathcal{B}_h(\boldsymbol{u}, \boldsymbol{v}) = \sum_{\ell=1}^{L} (\boldsymbol{\sigma}(\boldsymbol{u}), \boldsymbol{\epsilon}(\boldsymbol{v}))_{\Omega_\ell} - \langle \{\boldsymbol{\sigma}(\boldsymbol{u})\}, [\![\boldsymbol{v}]\!] \rangle_{\mathcal{F}_h^I} - \langle [\![\boldsymbol{u}]\!], \{\boldsymbol{\sigma}(\boldsymbol{v})\} \rangle_{\mathcal{F}_h^I} + \langle \eta [\![\boldsymbol{u}]\!], [\![\boldsymbol{v}]\!] \rangle_{\mathcal{F}_h^I}, \tag{7}$$

for any $\boldsymbol{u}, \boldsymbol{v} \in \boldsymbol{V}_h^N$ and where we have used the short-hand notation $\langle \boldsymbol{w}, \boldsymbol{v} \rangle_{\mathcal{F}_h^I} = \sum_{F \in \mathcal{F}_h^I} \langle \boldsymbol{w}, \boldsymbol{v} \rangle_F$. In (7) the facewise stabilization function $\eta \in L^\infty(\mathcal{F}_h^I)$ is defined as

$$\eta|_F = \alpha \{\boldsymbol{D}\}_H \frac{\max\{N_{\ell+}^2, N_{\ell-}^2\}}{\min\{h_{\ell+}, h_{\ell-}\}}, \quad \forall F \in \mathcal{F}_h^I,\ \overline{F} \subseteq \partial\overline{\Omega}_{\ell+} \cap \partial\overline{\Omega}_{\ell-}, \tag{8}$$

where α is a positive constant to be properly chosen and, for a piecewise constant tensor $\boldsymbol{D}$,

$$\{\boldsymbol{D}\}_H = 2 \frac{((\boldsymbol{n}^+)^T \boldsymbol{D}^+(\boldsymbol{n}^+))((\boldsymbol{n}^-)^T \boldsymbol{D}^-(\boldsymbol{n}^-))}{((\boldsymbol{n}^+)^T \boldsymbol{D}^+(\boldsymbol{n}^+)) + ((\boldsymbol{n}^-)^T \boldsymbol{D}^-(\boldsymbol{n}^-))}.$$

Remark 2.3. If $L = 1$, i.e., if there is only one subdomain and $\mathcal{F}_h^I = \emptyset$, formulation (5) corresponds to the classical spectral element method, see e.g. [20,21]. On the other hand, if Ω_ℓ for $\ell = 1, ..., L$ consists of only one element, the dG paradigm is employed elementwise.

We next introduce the following (mesh-dependent) norms

$$\begin{aligned} \|\boldsymbol{w}\|_*^2 &= \sum_{\ell=1}^{L} \|\mathbf{D}^{1/2}\boldsymbol{\epsilon}(\boldsymbol{w})\|^2_{\boldsymbol{\mathcal{L}}^2(\Omega_\ell)} + \|\eta^{1/2}[\![\boldsymbol{w}]\!]\|^2_{\boldsymbol{\mathcal{L}}^2(\mathcal{F}_h^I)} \quad \forall \boldsymbol{w} \in \boldsymbol{H}^1(\mathcal{T}_\Omega), \\ |||\boldsymbol{w}|||_*^2 &= \|\boldsymbol{w}\|_*^2 + \|\eta^{-1/2}\{\mathbf{D}\boldsymbol{\epsilon}(\boldsymbol{w})\}\|^2_{\boldsymbol{\mathcal{L}}^2(\mathcal{F}_h^I)} \quad \forall \boldsymbol{w} \in \boldsymbol{H}^2(\mathcal{T}_\Omega), \end{aligned} \tag{9}$$

with the convention that $\|\boldsymbol{w}\|^2_{\boldsymbol{\mathcal{L}}^2(\mathcal{F}_h^I)} = \sum_{F\in\mathcal{F}_h^I} \|\boldsymbol{w}\|^2_{\boldsymbol{\mathcal{L}}^2(F)}$. Using the trace-inverse inequalities [17,52,20] and Assumption 2.2, it can be proved that the norms $\|\cdot\|_*$ and $|||\cdot|||_*$ are equivalent when restricted to the space $\boldsymbol{V}_h^N$. The well-posedness of the semi-discrete formulation (5) follows from the following result, cf. [5] for the proof.

Proposition 1. *The bilinear form $\mathcal{B}_h(\cdot,\cdot) : \boldsymbol{V}_h^N \times \boldsymbol{V}_h^N \longrightarrow \mathbb{R}$ defined as in (7) satisfies*

$$|\mathcal{B}_h(\boldsymbol{w},\boldsymbol{v})| \lesssim \|\boldsymbol{w}\|_*\|\boldsymbol{v}\|_*, \quad \mathcal{B}_h(\boldsymbol{v},\boldsymbol{v}) \gtrsim \|\boldsymbol{v}\|_*^2 \quad \forall \boldsymbol{v},\boldsymbol{w} \in \boldsymbol{V}_h^N,$$

where the second estimate holds provided that the parameter α appearing in the definition of the stabilization function (8) is chosen sufficiently large. Moreover,

$$|\mathcal{B}_h(\boldsymbol{w},\boldsymbol{v})| \lesssim |||\boldsymbol{w}|||_*\|\boldsymbol{v}\|_* \forall \boldsymbol{w} \in \boldsymbol{H}^2(\mathcal{T}_h)\,, \forall \boldsymbol{v} \in \boldsymbol{V}_h^N.$$

We now recall the stability and convergence properties of the semi-discrete solution to (5). We refer the reader to [10] for the detailed proofs. For any real $s \geq 0$, we denote by $\boldsymbol{H}^s(\mathcal{T}_\Omega)$ the space of piecewise $\boldsymbol{H}^s$ vector-valued functions, we introduce the space-energy norm

$$\|\boldsymbol{w}\|_{\mathcal{E}}^2 = \|\sqrt{\rho}\dot{\boldsymbol{w}}\|^2_{\boldsymbol{L}^2(\Omega)} + \|\sqrt{\rho}\zeta\boldsymbol{w}\|^2_{\boldsymbol{L}^2(\Omega)} + \|\boldsymbol{w}\|_*^2 \quad \forall \boldsymbol{w} \in \boldsymbol{H}^1(\mathcal{T}_h) \tag{10}$$

and assess the following results.

Theorem 1. *[10, Theorem 3.3] For any time $t \in (0,T]$, let $\boldsymbol{u}_h(t) \in \boldsymbol{V}_h^N$ be the solution of problem (5). If $\boldsymbol{f} \in L^2(0,T;\boldsymbol{L}^2(\Omega))$, then*

$$\|\boldsymbol{u}_h(t)\|_{\mathcal{E}} \lesssim \|\boldsymbol{u}_h(0)\|_{\mathcal{E}} + \int_0^T \|\boldsymbol{f}(\tau)\|_{\boldsymbol{L}^2(\Omega)} d\tau, \quad 0 < t \leq T.$$

Theorem 2. *[10, Theorem 3.6] Assume that, for any time $t \in (0,T]$, the solution $\boldsymbol{u}(t)$ of problem (1) together with its two first temporal derivatives satisfy $\boldsymbol{u}(t)_{|\Omega_\ell}, \dot{\boldsymbol{u}}(t)_{|\Omega_\ell}, \ddot{\boldsymbol{u}}(t)_{|\Omega_\ell} \in \boldsymbol{H}^{s_\ell}(\Omega_\ell)$, $\ell = 1,\ldots,L$, $s_\ell \geq 2$. Let $\boldsymbol{u}_h(t)$ be the corresponding solution of the semi-discrete formulation (5) with a sufficiently large penalty parameter α in (8) and let $\boldsymbol{e}_h(t) = \boldsymbol{u}(t) - \boldsymbol{u}_h(t)$ for any $t \in (0,T]$. Then,*

$$\sup_{t\in[0,T]} \|\boldsymbol{e}_h(t)\|_{\mathcal{E}}^2 \lesssim \sum_{\ell=1}^{L} \frac{h_\ell^{2\beta_\ell-2}}{N_\ell^{2s_\ell-3}} \left(\sup_{t\in[0,T]} \mathcal{I}(\boldsymbol{u})(t) + \int_0^T \mathcal{I}(\dot{\boldsymbol{u}})(\tau)d\tau \right), \qquad \forall t \in (0,T],$$

where

$$\mathcal{I}(\boldsymbol{w}) = \|\dot{\boldsymbol{w}}\|^2_{H^{s_\ell}(\Omega_\ell)} + \|\boldsymbol{w}\|^2_{H^{s_\ell}(\Omega_\ell)}$$

and $\beta_\ell = \min\{s_\ell, N_\ell + 1\}$, for all $\ell = 1, ..., L$.

Now, we introduce the algebraic formulation of (5) that will be the starting point of the time discretization we will discuss in the next section. We denote by $N_{\text{dof}} = \dim(\boldsymbol{V}_h^N)$, by introducing a basis $\{\boldsymbol{\phi}_i\}_{i=1}^{N_{\text{dof}}}$ for $\boldsymbol{V}_h^N$, we write

$$\boldsymbol{u}_h(\boldsymbol{x},t) = \sum_{j=1}^{N_{\text{dof}}} U_j(t)\boldsymbol{\phi}_j(\boldsymbol{x}), \tag{11}$$

where $U_j(t)$ are the expansion coefficients of $\mathbf{u}_h(t)$ in the chosen basis. By taking $\boldsymbol{v} = \boldsymbol{\phi}_i$, $\forall i = 1,\ldots,N_{\text{dof}}$, in (5) and using (11) we obtain the following system of second-order differential equations

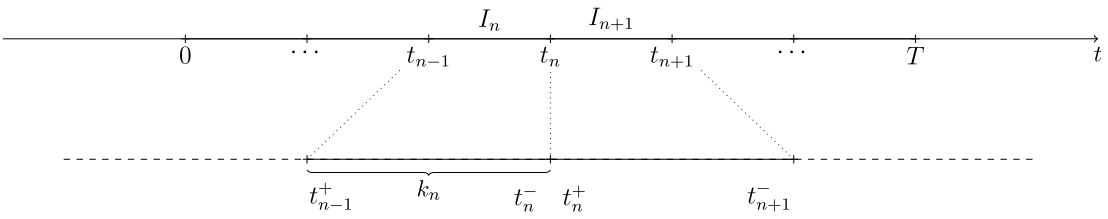

Fig. 2. Example of time domain partition (top). Zoom of the time domain partition: values t_n^+ and t_n^- are also reported (bottom).

$$M\ddot{\boldsymbol{U}}(t) + C\dot{\boldsymbol{U}}(t) + E\boldsymbol{U}(t) = \boldsymbol{F}(t), \tag{12}$$

with $\boldsymbol{U}(0) = \hat{\boldsymbol{U}}_0$ and $\dot{\boldsymbol{U}}(0) = \hat{\boldsymbol{U}}_1$, where $\boldsymbol{U}(t) \in \mathbb{R}^{N_{\text{dof}}}$ contains the expansion coefficients U_j in (11). The elements of the matrices M, C and E can be expressed as

$$M_{ij} = \sum_{\ell=1}^{L} (\rho \boldsymbol{\phi}_j, \boldsymbol{\phi}_i)_{\Omega_\ell}, \quad C_{ij} = \sum_{\ell=1}^{L} (2\rho\zeta \boldsymbol{\phi}_j, \boldsymbol{\phi}_i)_{\Omega_\ell}, \quad E_{ij} = \sum_{\ell=1}^{L} (\rho\zeta^2 \boldsymbol{\phi}_j, \boldsymbol{\phi}_i)_{\Omega_\ell} + \mathcal{B}_h(\boldsymbol{\phi}_j, \boldsymbol{\phi}_i), \tag{13}$$

for any $i, j = 1, ..., N_{\text{dof}}$, while the right-hand side $F_i(t) = \mathcal{F}_h(\boldsymbol{\phi}_i)$ for any $i = 1, ..., N_{\text{dof}}$.

Remark 2.4. Problem (12) is well posed and admits a unique solution $\mathbf{U} \in \mathbf{H}^2(0, T]$ in the interval $(0, T]$, provided that $\mathbf{F} \in \mathbf{L}^2(0, T]$, see [44].

2.2. dG time discretization

In this section we briefly review the time integration scheme introduced in [8] that is used for the time integration of the system (12). Notice that the following approach is independent from the choice of finite element discretization applied to the general problem (1).

We consider a partition $\mathcal{T}_k$ of the time interval $I = (0, T]$ made by N_T time-slabs such that $0 = t_0 < t_1 < \cdots < t_n < \cdots < t_{N_T} = T$ and define $I_n = (t_{n-1}, t_n]$ having length $k_n = t_n - t_{n-1}$, see Fig. 2. We define for (a regular enough function) $\boldsymbol{w}$, the time jump operator at t_n as

$$[\boldsymbol{w}]_n = \boldsymbol{w}(t_n^+) - \boldsymbol{w}(t_n^-), \qquad \text{for } n \geq 0,$$

where

$$\boldsymbol{w}(t_n^\pm) = \lim_{\epsilon \to 0^\pm} \boldsymbol{w}(t_n + \epsilon), \qquad \text{for } n \geq 0.$$

Moreover, we use the symbols $\boldsymbol{w}_n^+ = \boldsymbol{w}(t_n^+)$ and $\boldsymbol{w}_n^- = \boldsymbol{w}(t_n^-)$ to represent the trace of (a regular enough) $\boldsymbol{w}$, taken with the interior of I_{n+1} and I_n, respectively. Finally, we introduce the functional spaces

$$\boldsymbol{W}_{k_n}^{r_n} = \{\boldsymbol{w} : I_n \to \mathbb{R}^{N_{\text{dof}}} : \boldsymbol{w} \in [\mathbb{P}^{r_n}(I_n)]^{N_{\text{dof}}}\},$$

and

$$\boldsymbol{W}_k^r = \{\boldsymbol{w} \in \boldsymbol{L}^2(0, T) : \boldsymbol{w}|_{I_n} \in \boldsymbol{W}_{k_n}^{r_n} \ \forall n = 1, \ldots, N_T\}.$$

Next, by multiplying equation (12) by a test function $\boldsymbol{V} \in \boldsymbol{W}_k^r$ and integrating it with respect to time we obtain the problem: find $\boldsymbol{U}_k \in \boldsymbol{W}_k^r$ such that

$$\begin{aligned} &\sum_{n=1}^{N_T} \left[(M\ddot{\boldsymbol{U}}_k, \dot{\boldsymbol{V}})_{I_n} + (C\dot{\boldsymbol{U}}_k, \dot{\boldsymbol{V}})_{I_n} + (E\boldsymbol{U}_k, \dot{\boldsymbol{V}})_{I_n} \right] + \sum_{n=1}^{N_T - 1} \left[M[\dot{\boldsymbol{U}}_k]_n \cdot \dot{\boldsymbol{V}}(t_n^+) + E[\boldsymbol{U}_k]_n \cdot \boldsymbol{V}(t_n^+) \right] \\ &\quad + M\dot{\boldsymbol{U}}_k(0^+) \cdot \dot{\boldsymbol{V}}(0^+) + E\boldsymbol{U}_k(0^+) \cdot \boldsymbol{V}(0^+) = \sum_{n=1}^{N_T} (\boldsymbol{F}, \dot{\boldsymbol{V}})_{I_n} + M\hat{\boldsymbol{U}}_1 \cdot \dot{\boldsymbol{V}}(0^+) + E\hat{\boldsymbol{U}}_0 \cdot \boldsymbol{V}(0^+), \end{aligned} \tag{14}$$

for any $\boldsymbol{V} \in \boldsymbol{W}_k^r$. Note that, thanks to the regularity assumption on $\mathbf{U}$, cf. Remark 2.4, we added to (12) the null terms $E[\mathbf{U}]_n$ and $[\dot{\mathbf{U}}]_n$ for any $n = 1, ..., N_T$, see also [8]. Finally, we recall the following stability and convergence results of the time discretization (14). We refer the reader to [8] for an exhaustive analysis of the method and for the complete proofs of the main results. We firstly introduce the energy norm

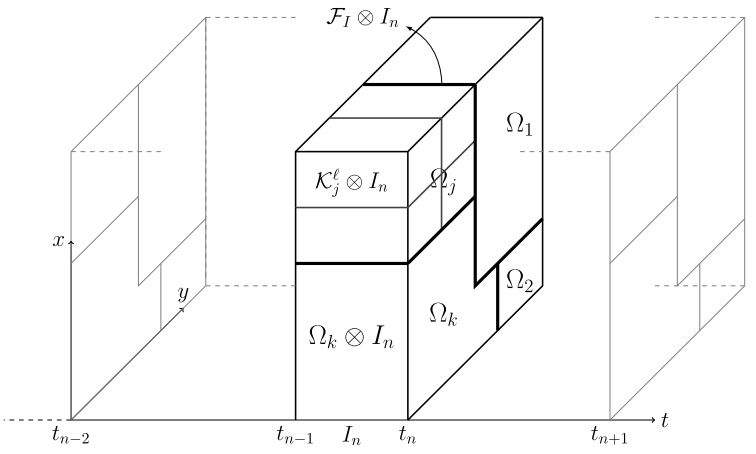

Fig. 3. Example of space-time domain partition $\mathcal{T}$ obtained as the tensor product of space and time mesh grids $\mathcal{T}_h$ and $\mathcal{T}_k$, cf. Fig. 1 and Fig. 2, respectively. The general element mesh $\mathcal{K}_\ell^j \otimes I_n \in \mathcal{T}$ is also reported.

$$||\boldsymbol{W}||_E = \sum_{n=1}^{N_T} ||C^{1/2}\dot{\boldsymbol{W}}||_{\boldsymbol{L}^2(I_n)} + \frac{1}{2}(M^{1/2}\dot{\boldsymbol{W}}(0+))^2 + \frac{1}{2}\sum_{n=1}^{N_T}(M^{1/2}[\dot{\boldsymbol{W}}]_n)^2 + \frac{1}{2}(M^{1/2}\dot{\boldsymbol{W}}(T^-))^2 + \frac{1}{2}(E^{1/2}\boldsymbol{W}(0^+))^2 + \frac{1}{2}\sum_{n=1}^{N_T}(E^{1/2}[\boldsymbol{W}]_n)^2 + \frac{1}{2}(E^{1/2}\boldsymbol{W}(T^-))^2, \tag{15}$$

for any $\boldsymbol{W} \in \boldsymbol{W}_k^r$.

Theorem 3. *[8, Proposition 3] Let $\boldsymbol{F} \in \boldsymbol{L}^2(0,T]$ and $\hat{\boldsymbol{U}}_0, \hat{\boldsymbol{U}}_1 \in \mathbb{R}^{N_{\text{dof}}}$. Then, the solution $\boldsymbol{U}_k \in \boldsymbol{W}_k^r$ of (14) satisfies*

$$||\boldsymbol{U}_k||_E \lesssim \left(||C^{1/2}\boldsymbol{F}||^2_{\boldsymbol{L}^2(0,T)} + (E^{1/2}\hat{\boldsymbol{U}}_0)^2 + (M^{1/2}\hat{\boldsymbol{U}}_1)^2 \right)^{\frac{1}{2}}.$$

Theorem 4. *Let $\boldsymbol{U}$ be the solution of (12) such that $\boldsymbol{U}|_{I_n} \in \boldsymbol{H}^{q_n}(I_n)$, for any $n = 1, \dots, N_T$ with $q_n \geq 2$, and let $\boldsymbol{U}_k \in \boldsymbol{W}_k^r$ be the solution of (14). Then, it holds*

$$||\boldsymbol{U} - \boldsymbol{U}_k||_E^2 \lesssim \sum_{n=1}^{N_T} \frac{k_n^{2\beta_n - 3}}{r_n^{2q_n - 6}} ||\boldsymbol{U}||_{\boldsymbol{H}^{q_n}(I_n)}, \tag{16}$$

where $\beta_n = \min\{r_n + 1, q_n\}$, for any $n = 1, \dots, N_T$, and the hidden constants depend on the infinity norm of the matrices M, C and E.

2.3. dG space-time discretization

In this section we present a space-time discontinuous Galerkin approximation that combine the discretization techniques described in Section 2.1 and Section 2.2. We consider a domain partition $\mathcal{T}$ of the domain $Q = \Omega \times I$ obtained as the tensor product of space and time mesh grids, i.e., $\mathcal{T} = \mathcal{T}_h \otimes \mathcal{T}_k$. The general mesh element $Q_{\ell n} \in \mathcal{T}$ is a polytope of the form $Q_{\ell,n} = \mathcal{K}_\ell^j \otimes I_n$ where $\mathcal{K}_\ell^j$ is either a tetrahedron (resp. triangle) or a hexahedron (resp. square) in $\Omega_\ell \subset \mathcal{T}_h$ and I_n is the $n-th$ time-slab. Notice that within this discretization we can allow for discontinuous approximation both in the space domain, i.e., across the hypersurface $\mathcal{F}_I \otimes I_n$ for $n = 1, ..., N_T$, and in the time domain, i.e., along the interface $\mathcal{T}_h \otimes \{t_n\}$ for any $n = 1, ..., N_T$. A sketch of a three dimensional (space-time) domain discretization is represented in Fig. 3.

The space-time dG finite element space $\mathcal{V}_{DG} = \boldsymbol{V}_h^N \otimes \boldsymbol{W}_k^r$ is defined based on the previous domain decomposition in the following way

$$\mathcal{V}_{DG} = \{\boldsymbol{w}(\boldsymbol{x},t) = \boldsymbol{w}_1(\boldsymbol{x})w_2(t) : \mathcal{T}_h \times \mathcal{T}_k \to \mathbb{R}^3 : \boldsymbol{w}_1(\boldsymbol{x}) \in \boldsymbol{V}_h^N \text{ and } w_2(t) \in \boldsymbol{W}_k^r\}. \tag{17}$$

Now, we consider the first equation in (1) in the cylinder $Q_{\ell,n} = \Omega_\ell \otimes I_n$, we multiply it by a test function $\dot{\boldsymbol{v}}$, with $\boldsymbol{v} \in \mathcal{V}_{DG}$ and integrate in space and time over the cylinder $Q_{\ell,n}$, obtaining

$$(\rho\ddot{\boldsymbol{u}}, \dot{\boldsymbol{v}})_{Q_{\ell,n}} + (2\rho\zeta\dot{\boldsymbol{u}}, \dot{\boldsymbol{v}})_{Q_{\ell,n}} + (\rho\zeta^2\boldsymbol{u}, \dot{\boldsymbol{v}})_{Q_{\ell,n}} - (\nabla \cdot \boldsymbol{\sigma}(\boldsymbol{u}), \dot{\boldsymbol{v}})_{Q_{\ell,n}} = (\boldsymbol{f}, \dot{\boldsymbol{v}})_{Q_{\ell,n}}. \tag{18}$$

Next, being $\mathbf{u} \in C^1(0,T;\mathbf{L}^2(\Omega))$ we add the null terms

$$(\rho[\dot{\boldsymbol{u}}]_{n-1}, \dot{\boldsymbol{v}}(t_{n-1}^+))_\Omega, \quad (\rho\zeta^2[\boldsymbol{u}]_{n-1}, \boldsymbol{v}(t_{n-1}^+))_\Omega, \quad (\boldsymbol{\sigma}([\boldsymbol{u}]_{n-1}), \boldsymbol{\epsilon}(\boldsymbol{v}(t_{n-1}^+)))_\Omega, \tag{19}$$

we integrate by parts with respect to both space and time variables over $Q_{\ell n}$ and we sum up over all time slabs and all subdomains obtaining: find $\boldsymbol{u}_{DG} \in \mathcal{V}_{DG}$ such that

$$\mathcal{A}(\boldsymbol{u}_{DG}, \boldsymbol{v}) = \mathcal{F}(\boldsymbol{v}) \quad \forall \boldsymbol{v} \in \mathcal{V}_{DG}, \tag{20}$$

where

$$\begin{aligned}
\mathcal{A}(\boldsymbol{w}, \boldsymbol{v}) = &\sum_{n=1}^{N_T}\sum_{\ell=1}^{L}\Big[(\rho \boldsymbol{w}_1\ddot{w}_2, \boldsymbol{v}_1\dot{v}_2)_{Q_{\ell n}} + (2\rho\zeta \boldsymbol{w}_1\dot{w}_2, \boldsymbol{v}_1\dot{v}_2)_{Q_{\ell n}} + (\rho\zeta^2 \boldsymbol{w}_1 w_2, \boldsymbol{v}_1\dot{v}_2)_{Q_{\ell n}}\Big] \\
&+ \sum_{n=1}^{N_T}\mathcal{B}_h(\boldsymbol{w}_1, \boldsymbol{v}_1)(w_2, \dot{v}_2)_{I_n} + \sum_{n=1}^{N_T-1}\mathcal{B}_h(\boldsymbol{w}_1, \boldsymbol{v}_1)[w_2]_n v_2(t_n^+) + \mathcal{B}_h(\boldsymbol{w}_1, \boldsymbol{v}_1)w_2(0^+)v_2(0^+) \\
&+ \sum_{n=1}^{N_T-1}\sum_{\ell=1}^{L}\Big[(\rho \boldsymbol{w}_1, \boldsymbol{v}_1)_{\Omega_\ell}[\dot{w}_2]_n \dot{v}_2(t_n^+) + (\rho\zeta^2 \boldsymbol{w}_1, \boldsymbol{v}_1)_{\Omega_\ell}[w_2]_n v_2(t_n^+)\Big] \\
&+ \sum_{\ell=1}^{L}\Big[(\rho \boldsymbol{w}_1, \boldsymbol{v}_1)_{\Omega_\ell}\dot{w}_2(0^+)\dot{v}_2(0^+) + (\rho\zeta^2 \boldsymbol{w}_1, \boldsymbol{v}_1)_{\Omega_\ell} w_2(0^+)v_2(0^+)\Big],
\end{aligned} \tag{21}$$

and

$$F(\boldsymbol{v}) = \sum_{n=1}^{N_T}\sum_{\ell=1}^{L}(\boldsymbol{f}, \boldsymbol{v}_1\dot{v}_2)_{Q_{n\ell}} + \sum_{\ell=1}^{L}\Big[(\rho\hat{\boldsymbol{u}}_1, \boldsymbol{v}_1)_{\Omega_\ell}\dot{v}_2(0^+) + (\rho\zeta^2\hat{\boldsymbol{u}}_0, \boldsymbol{v}_1)_{\Omega_\ell}v_2(0^+)\Big] + \mathcal{B}_h(\hat{\boldsymbol{u}}_0, \boldsymbol{v}_1)v_2(0^+), \tag{22}$$

for any $\boldsymbol{w}, \boldsymbol{v} \in \mathcal{V}_{DG}$.

In view of the forthcoming analysis we state the following result.

Proposition 2. *The function* $|||\cdot||| : H^2(0,T;\mathbf{H}^1_{0,\Gamma_D}(\Omega)) \to \mathbb{R}^+$ *defined as*

$$|||\boldsymbol{w}|||^2 = \frac{1}{2}\|\boldsymbol{w}(0^+)\|_{\mathcal{E}}^2 + \frac{1}{2}\sum_{n=1}^{N_T-1}\|[\boldsymbol{w}]_n\|_{\mathcal{E}}^2 + \frac{1}{2}\|\boldsymbol{w}(T^-)\|_{\mathcal{E}}^2 + \sum_{n=1}^{N_T}||\sqrt{2\rho\zeta}\,\dot{\boldsymbol{w}}||^2_{\mathbf{L}^2(Q_n)} \tag{23}$$

is a norm on $H^2(0,T;\mathbf{H}^1_{0,\Gamma_D}(\Omega))$.

Proof. It is clear that homogeneity and subadditivity hold, since $|||\cdot|||$ is the combination of norms. Therefore, we have only to show that $|||\boldsymbol{w}||| = 0 \iff \boldsymbol{w} = \mathbf{0}\ \forall \boldsymbol{w} \in H^2(0,T;\mathbf{H}^1_{0,\Gamma_D}(\Omega))$.
If $\boldsymbol{w} = \mathbf{0}$, it is immediate that $|||\boldsymbol{w}||| = 0$. Then, suppose that $|||\boldsymbol{w}||| = 0$. This implies that all the terms on the right hand side of (23) are null. Therefore, we have that

$$||\sqrt{2\rho\zeta}\,\dot{\boldsymbol{w}}(t)||^2_{\mathbf{L}^2(Q_n)} = 0 \quad \forall n = 1, \dots, N_T,$$

that means $\partial_t \boldsymbol{w}(\boldsymbol{x},t) = \mathbf{0}$ on each Q_n. In addition, from

$$||\sqrt{\rho\zeta^2}\,\boldsymbol{w}(0^+)||^2_{\mathbf{L}^2(\Omega)} = 0,$$

we have that $\boldsymbol{w}(\boldsymbol{x},0^+) = \mathbf{0}$. It follows that $\boldsymbol{w}$ satisfies

$$\begin{cases} \partial_t \boldsymbol{w}(\boldsymbol{x},t) = \mathbf{0} & \text{on } Q_1, \\ \boldsymbol{w}(\boldsymbol{x},0^+) = \mathbf{0}, \end{cases}$$

and so $\boldsymbol{w} = \mathbf{0}$ on Q_1. We proceed by induction and suppose $\boldsymbol{w}(\boldsymbol{x},t) = \mathbf{0}$ on Q_{n-1}. Using that

$$||\sqrt{\rho\zeta^2}[\boldsymbol{w}]_n||^2_{\mathbf{L}^2(\Omega)} = 0 \quad \forall n = 1, \dots, N_T - 1,$$

in (23), cf. also (10), and the induction assumption, we obtain

$$0 = [\boldsymbol{w}]_n = \boldsymbol{w}(\boldsymbol{x}, t_{n-1}^+) - \boldsymbol{w}(\boldsymbol{x}, t_{n-1}^-) = \boldsymbol{w}(\boldsymbol{x}, t_{n-1}^+)$$

Therefore, once again we have that

$$\begin{cases} \partial_t \boldsymbol{w}(\boldsymbol{x},t) = \boldsymbol{0} & \text{on } Q_n, \\ \boldsymbol{w}(\boldsymbol{x},t_{n-1}^+) = \boldsymbol{0}, \end{cases}$$

and so $\boldsymbol{w} = \boldsymbol{0}$ on Q_n $\forall n = 1,\dots,N_T-1$. □

Remark 2.5. If $\boldsymbol{w} \in \mathcal{V}_{DG}$ then we can write the energy norm (23) as

$$|||\boldsymbol{w}|||^2 = \mathcal{N}(\dot{w}_2)||\sqrt{\rho}\boldsymbol{w}_1||^2_{\mathbf{L}^2(\Omega)} + \sum_{n=1}^{N_T} ||\dot{w}_2||^2_{\mathbf{L}^2(I_n)}||\sqrt{2\rho\zeta}\,\boldsymbol{w}_1||^2_{\mathbf{L}^2(\Omega)} + \mathcal{N}(w_2)\left[||\sqrt{\rho\zeta^2}\boldsymbol{w}_1||^2_{\mathbf{L}^2(\Omega)} + \|\boldsymbol{w}\|^2_*\right], \tag{24}$$

where

$$\mathcal{N}(w) = \frac{1}{2}w(T^-)^2 + \frac{1}{2}w(0^+)^2 + \frac{1}{2}\sum_{n=1}^{N_T-1}([w]_n)^2. \tag{25}$$

We are next ready to prove that (20) is well-posed.

Theorem 5 *(Well-posedness). Problem (20) admits a unique solution, provided that the stabilization parameter α in (8) is chosen large enough.*

Proof. We first show that $\mathcal{A}(\cdot,\cdot)$ is coercive w.r.t. the energy norm (10). Taking $\boldsymbol{u} = \boldsymbol{u}_1 u_2 \in \mathcal{V}_{DG}$, we have

$$\begin{aligned}
\mathcal{A}(\boldsymbol{u},\boldsymbol{u}) = {} & \underbrace{\sum_{n=1}^{N_T}\sum_{\ell=1}^{L}\left[(\rho\boldsymbol{u}_1\ddot{u}_2, \boldsymbol{u}_1\dot{u}_2)_{Q_{\ell n}}\right]}_{T_1} + \underbrace{\sum_{n=1}^{N_T}\sum_{\ell=1}^{L}\left[(2\rho\zeta\boldsymbol{u}_1\dot{u}_2, \boldsymbol{u}_1\dot{u}_2)_{Q_{\ell n}}\right]}_{T_2} + \underbrace{\sum_{n=1}^{N_T}\sum_{\ell=1}^{L}\left[(\rho\zeta^2\boldsymbol{u}_1 u_2, \boldsymbol{u}_1\dot{u}_2)_{Q_{\ell n}}\right]}_{T_3} \\
& + \underbrace{\sum_{n=1}^{N_T}\mathcal{B}_h(\boldsymbol{u}_1,\boldsymbol{u}_1)(u_2,\dot{u}_2)_{I_n}}_{T_4} + \underbrace{\sum_{n=1}^{N_T-1}\mathcal{B}_h(\boldsymbol{u}_1,\boldsymbol{u}_1)[u_2]_n u_2(t_n^+)}_{T_5} + \underbrace{\mathcal{B}_h(\boldsymbol{u}_1,\boldsymbol{u}_1)u_2(0^+)^2}_{T_6} \\
& + \underbrace{\sum_{n=1}^{N_T-1}\sum_{\ell=1}^{L}\left[(\rho\boldsymbol{u}_1,\boldsymbol{u}_1)_{\Omega_\ell}[\dot{u}_2]_n\dot{u}_2(t_n^+)\right]}_{T_7} + \underbrace{\sum_{n=1}^{N_T-1}\sum_{\ell=1}^{L}(\rho\zeta^2\boldsymbol{u}_1,\boldsymbol{u}_1)_{\Omega_\ell}[u_2]_n u_2(t_n^+)}_{T_8} \\
& + \underbrace{\sum_{\ell=1}^{L}(\rho\boldsymbol{u}_1,\boldsymbol{u}_1)_{\Omega_\ell}\dot{u}_2(0^+)^2}_{T_9} + \underbrace{(\rho\zeta^2\boldsymbol{u}_1,\boldsymbol{u}_1)_{\Omega_\ell}u_2(0^+)^2}_{T_{10}}
\end{aligned}$$

Integrating by parts with respect to time the term T_1 we obtain

$$\begin{aligned}
\sum_{n=1}^{N_T}\sum_{\ell=1}^{L}(\rho\boldsymbol{u}_1\ddot{u}_2,\boldsymbol{u}_1\dot{u}_2)_{Q_{\ell n}} &= \sum_{\ell=1}^{L}\|\sqrt{\rho}\boldsymbol{u}_1\|^2_{\mathbf{L}^2(\Omega_\ell)}\sum_{n=1}^{N_T}\left[-(\dot{u}_2,\ddot{u}_2)_{I_n} + \dot{u}_2(t_n^-)^2 - \dot{u}_2(t_{n-1}^+)^2\right] \\
&= \sum_{\ell=1}^{L}\|\sqrt{\rho}\boldsymbol{u}_1\|^2_{\mathbf{L}^2(\Omega_\ell)}\sum_{n=1}^{N_T}\left[\frac{1}{2}\dot{u}_2(t_n^-)^2 - \frac{1}{2}\dot{u}_2(t_{n-1}^+)^2\right],
\end{aligned}$$

and summing it up with T_7 and T_9 we have

$$T_1 + T_7 + T_9 = \sum_{\ell=1}^{L}\|\sqrt{\rho}\boldsymbol{u}_1\|^2_{\mathbf{L}^2(\Omega_\ell)}\left[\frac{1}{2}\dot{u}_2(0^+)^2 + \frac{1}{2}\sum_{n=1}^{N_T-1}([\dot{u}_2])_n^2 + \frac{1}{2}\dot{u}_2(T^-)^2\right].$$

Then, we integrate by parts T_3 and sum it with T_8 and T_{10} obtaining

$$T_3 + T_8 + T_{10} = \sum_{\ell=1}^{L}\|\sqrt{\rho\zeta^2}\boldsymbol{u}_1\|^2_{\mathbf{L}^2(\Omega_\ell)}\left[\frac{1}{2}u_2(0^+)^2 + \frac{1}{2}\sum_{n=1}^{N_T-1}([u_2])_n^2 + \frac{1}{2}u_2(T^-)^2\right],$$

and, similarly, for T_4, T_5 and T_6 we obtain

$$T_4+T_5+T_6=\sum_{n=1}^{N_T}\mathcal{B}_h(\boldsymbol{u}_1,\boldsymbol{u}_1)(u_2,\dot{u}_2)_{I_n}+\sum_{n=1}^{N_T-1}\mathcal{B}_h(\boldsymbol{u}_1,\boldsymbol{u}_1)[u_2]_n u_2(t_n^+)+\mathcal{B}_h(\boldsymbol{u}_1,\boldsymbol{u}_1)u_2(0^+)^2$$
$$=\mathcal{B}_h(\boldsymbol{u}_1,\boldsymbol{u}_1)\left[\frac{1}{2}u_2(0^+)^2+\frac{1}{2}\sum_{n=1}^{N_T-1}[u_2]_n^2+\frac{1}{2}u_2(T^-)^2\right].$$

Now, using the coercivity of the bilinear form $\mathcal{B}_h(\cdot,\cdot)$, of Proposition 1, and definition (25), we obtain

$$\mathcal{A}(\boldsymbol{u},\boldsymbol{u})\gtrsim\mathcal{N}(\dot{u}_2)\|\sqrt{\rho}\boldsymbol{u}_1\|^2_{\mathbf{L}^2(\Omega)}+\sum_{n=1}^{N_T}\|\dot{u}_2\|^2_{L^2(I_n)}\|\sqrt{2\rho\zeta}\boldsymbol{u}_1\|^2_{\mathbf{L}^2(\Omega)}+\mathcal{N}(u_2)\left[\|\sqrt{\rho\zeta^2}\boldsymbol{u}_1\|^2_{\mathbf{L}^2(\Omega)}+\|\boldsymbol{u}_1\|^2_*\right]=|||\boldsymbol{u}|||^2.$$

We now prove the continuity of $\mathcal{F}(\cdot)$. Using definition (22), the arithmetic-geometric inequality and the Cauchy-Schwartz inequality we have that

$$|\mathcal{F}(\boldsymbol{v})|^2\lesssim\|(2\rho\zeta)^{-\frac{1}{2}}\boldsymbol{f}\|^2_{\mathbf{L}^2(Q)}\|\sqrt{2\rho\zeta}\boldsymbol{v}_1\|^2_{\mathbf{L}^2(\Omega)}\sum_{n=1}^{N_T}\|\dot{v}_2\|^2_{L^2(I_n)}+\|\hat{\boldsymbol{u}}_1\|^2_{\mathbf{L}^2(\Omega)}\|\sqrt{\rho}\boldsymbol{v}_1\|^2_{\mathbf{L}^2(\Omega)}\dot{v}_2(0^+)^2$$
$$+\left[\|\hat{\boldsymbol{u}}_0\|^2_{\mathbf{L}^2(\Omega)}\|\sqrt{\rho\zeta^2}\boldsymbol{v}_1\|^2_{\mathbf{L}^2(\Omega)}+\mathcal{B}_h(\hat{\boldsymbol{u}}_0,\boldsymbol{v}_1)^2\right]v_2(0^+)^2\quad\forall\,\boldsymbol{v}=\boldsymbol{v}_1v_2\in\mathcal{V}_{DG}.$$

Now, using the continuity of $\mathcal{B}_h(\cdot,\cdot)$ in Proposition 1, i.e.,

$$|\mathcal{B}_h(\hat{\boldsymbol{u}}_0,\boldsymbol{v}_1)|\lesssim\left|\left|\left|\hat{\boldsymbol{u}}_0\right|\right|\right|_*\|\boldsymbol{v}_1\|_*$$

we can easily obtain

$$|\mathcal{F}(\boldsymbol{v})|\lesssim\left[\|(2\rho\zeta)^{-\frac{1}{2}}\boldsymbol{f}\|^2_{\mathbf{L}^2(Q)}+\|\hat{\boldsymbol{u}}_1\|^2_{\mathbf{L}^2(\Omega)}+\|\hat{\boldsymbol{u}}_0\|^2_{\mathbf{L}^2(\Omega)}+\left|\left|\left|\hat{\boldsymbol{u}}_0\right|\right|\right|_*\right]^{\frac{1}{2}}|||\boldsymbol{v}|||,$$

and this concludes the proof. □

As a direct consequence of the previous theorem we have the following result

Theorem 6 *(Stability). Let $\boldsymbol{u}_{DG}\in\mathcal{V}_{DG}$ be the solution of (20) and let $\boldsymbol{f}\in C^1((0,T];\boldsymbol{L}^2(\Omega))$, $\hat{\mathbf{u}}_0\in\mathbf{H}^1_{0,\Gamma_D}(\Omega)\cap\mathbf{H}^{\Delta}_{\boldsymbol{D}}(\Omega)$ and $\hat{\mathbf{u}}_1\in\mathbf{H}^1_{0,\Gamma_D}(\Omega)$. Then, it holds*

$$|||\boldsymbol{u}_{DG}|||^2\lesssim\|(2\rho\zeta)^{-\frac{1}{2}}\boldsymbol{f}\|^2_{\mathbf{L}^2(Q)}+\|\hat{\boldsymbol{u}}_1\|^2_{\mathbf{L}^2(\Omega)}+\|\hat{\boldsymbol{u}}_0\|^2_{\mathbf{L}^2(\Omega)}+\left|\left|\left|\hat{\boldsymbol{u}}_0\right|\right|\right|_*,\tag{26}$$

where the hidden constant is independent of the discretization parameters.

Proof. The proof follows from the coercivity of the bilinear form $\mathcal{A}(\cdot,\cdot)$ and the continuity of the linear functional $\mathcal{F}(\cdot)$. □

3. Algebraic formulation

We derive here the algebraic formulation corresponding to problem (20) for the time slab I_n, $n=1,\dots,N_T-1$. Notice that the employment of discontinuous approximation between different hypersurfaces $\mathcal{T}_h\otimes\{t_n\}$ allows to compute the solution of the problem separately for one time slab at a time. Indeed, the weak formulation (20) restricted to I_n reads as: find $\boldsymbol{u}^n_{DG}\equiv\boldsymbol{u}_{DG|_{I_n}}\in V_h^N\times\mathbf{W}^{r_n}_{k_n}$ such that

$$\mathcal{A}_n(\boldsymbol{u}^n_{DG},\boldsymbol{v})=\mathcal{F}_n(\boldsymbol{v})\quad\forall\boldsymbol{v}\in V_h^N\times\mathbf{W}^{r_n}_{k_n},\tag{27}$$

where

$$\mathcal{A}_n(\boldsymbol{w},\boldsymbol{v})=\sum_{\ell=1}^{L}\left[(\rho\boldsymbol{w}_1,\boldsymbol{v}_1)_{\Omega_\ell}(\ddot{w}_2,\dot{v}_2)_{I_n}+(2\rho\zeta\boldsymbol{w}_1,\boldsymbol{u}_1)_{\Omega_\ell}(\dot{w}_2,\dot{v}_2)_{I_n},+(\rho\zeta^2\boldsymbol{w}_1,\boldsymbol{v}_1)_{\Omega_\ell}(w_2,\dot{v}_2)_{I_n}\right]$$
$$+\mathcal{B}_h(\boldsymbol{w}_1,\boldsymbol{v}_1)(w_2,\dot{v}_2)_{I_n}+\mathcal{B}_h(\boldsymbol{w}_1,\boldsymbol{v}_1)w_2(t^+_{n-1})v_2(t^+_{n-1})\tag{28}$$
$$+\sum_{\ell=1}^{L}\left[(\rho\boldsymbol{w}_1,\boldsymbol{v}_1)_{\Omega_\ell}\dot{w}_2(t^+_{n-1})\dot{v}_2(t^+_{n-1})+(\rho\zeta^2\boldsymbol{w}_1,\boldsymbol{v}_1)_{\Omega_\ell}w_2(t^+_{n-1})v_2(t^+_{n-1})\right],$$

for any $\boldsymbol{w}, \boldsymbol{v} \in V_h^N \times \mathbf{W}_{k_n}^{r_n}$ and

$$F_n(\boldsymbol{v}) = \sum_{\ell=1}^{L} (\boldsymbol{f}, \boldsymbol{v}_1 \dot{v}_2)_{Q_{\ell n}} + \sum_{\ell=1}^{L} \Big[(\rho \dot{\boldsymbol{u}}(t_{n-1}^-), \boldsymbol{v}_1)_{\Omega_\ell} \dot{v}_2(t_{n-1}^+) + (\rho \zeta^2 \boldsymbol{u}(t_{n-1}^-), \boldsymbol{v}_1)_{\Omega_\ell} v_2(t_{n-1}^+) \Big] + \mathcal{B}_h(\boldsymbol{u}(t_{n-1}^-), \boldsymbol{v}_1) v_2(t_{n-1}^+), \tag{29}$$

for any $\boldsymbol{v} \in V_h^N \times \mathbf{W}_{k_n}^{r_n}$. Notice that in (29) the values $\dot{\boldsymbol{u}}(t_{n-1}^-)$ and $\boldsymbol{u}(t_{n-1}^-)$ computed for I_{n-1} are used as initial conditions for the current slab. Notice also that, for the slab I_1, we set $\dot{\boldsymbol{u}}_1(t_0^-) = \hat{\boldsymbol{u}}_1$ and $\boldsymbol{u}_1(t_0^-) = \hat{\boldsymbol{u}}_0$. Let us set a basis $\{\boldsymbol{\phi}_i(\boldsymbol{x})\psi^\ell(t)\}$ for $V_h^N \times \mathbf{W}_{k_n}^{r_n}$, where $\{\boldsymbol{\phi}_i(\boldsymbol{x})\}_{i=1}^{N_{\text{dof}}}$, resp. $\{\psi^\ell(t)\}_{\ell=1}^{r_n+1}$ is basis for $\boldsymbol{V}_h^N$, resp. $\mathbf{W}_{k_n}^{r_n}$, and fix $D = N_{\text{dof}}(r_n+1)$. Then, we can write the trial function $\boldsymbol{u}_{DG}$ as a linear combination of the basis functions, i.e.,

$$\boldsymbol{u}_{DG}(\boldsymbol{x}, t) = \sum_{j=1}^{Ndof} \sum_{m=1}^{r_n+1} \alpha_j^m \boldsymbol{\phi}_j(\boldsymbol{x}) \psi^m(t),$$

where $\alpha_j^m \in \mathbb{R}$ for $j = 1, \dots, N_{\text{dof}}$ and $m = 1, \dots, r_n+1$. Next, we write equation (27) for any test function $\boldsymbol{\phi}_i(\boldsymbol{x})\psi^\ell(t)$, $i = 1, \dots, N_{\text{dof}}$, $\ell = 1, \dots, r_n+1$, obtaining the algebraic system

$$A_n \boldsymbol{\alpha}_n = \mathbf{F}_n, \tag{30}$$

where on the interval I_n, $A_n \in \mathbb{R}^{D\times D}$ is the associated local stiffness matrices, $\boldsymbol{\alpha}_n \in \mathbb{R}^D$ the solution vector and $\mathbf{F}_n \in \mathbb{R}^D$ corresponds to the data. We next investigate the structure of the matrix A_n by defining the following local matrices for $\ell, m = 1, \dots, r_n+1$,

$$N_1^{\ell m} = (\ddot{\psi}^m, \dot{\psi}^\ell)_{I_n}, \qquad N_2^{\ell m} = (\dot{\psi}^m, \dot{\psi}^\ell)_{I_n}, \qquad N_3^{\ell m} = (\psi^m, \dot{\psi}^\ell)_{I_n},$$
$$N_4^{\ell m} = \dot{\psi}^m(t_{n-1}^+)\dot{\psi}^\ell(t_{n-1}^+), \quad N_5^{\ell m} = \psi^m(t_{n-1}^+)\psi^\ell(t_{n-1}^+).$$

Then, by using equation (28) we can write

$$A_n = M \otimes (N_1 + N_4) + C \otimes N_2 + E \otimes (N_3 + N_5),$$

where M, C and E are defined in (13) and $A \otimes B$ denotes the Kronecher tensor product between the matrix A and the matrix B. On the other hand, the right-hand side $\mathbf{F}_n$ can be expressed as $\mathbf{F}_n = [F_{1,1}, \dots, F_{1,r_n+1}, F_{2,1}, \dots, F_{2,r_n+1}, \dots, F_{N_{\text{dof}},1}, \dots, F_{N_{\text{dof}},r_n+1}]^T$, where

$$F_{i,k} = \sum_{\ell=1}^{L} (\boldsymbol{f}, \boldsymbol{\phi}_i \dot{\psi}^k)_{Q_{\ell n}} + \sum_{\ell=1}^{L} \Big[(\rho \dot{\boldsymbol{u}}_{DG}(t_{n-1}^-), \boldsymbol{\phi}_i)_{\Omega_\ell} \dot{\psi}^k(t_{n-1}^+) + (\rho \zeta^2 \boldsymbol{u}_{DG}(t_{n-1}^-), \boldsymbol{\phi}_i)_{\Omega_\ell} \psi^k(t_{n-1}^+) \Big] + \mathcal{B}_h(\boldsymbol{u}_{DG}(t_{n-1}^-), \boldsymbol{\phi}_i) \psi^k(t_{n-1}^+),$$

for any $i = 1, \dots, N_{\text{dof}}$ and $k = 1, \dots, r_n+1$. We remark that the matrix A_n associated to the linear system (30) is skew symmetric and, in the general case, has to be built for any time slab I_n. However, if the time discretization parameter are fix, i.e., the time integration step $k_n = k$ and the polynomial degree $r_n = r$ for any $n = 1, \dots, N_T - 1$, then the matrix A_n can be stored and factorized once and for all, at the beginning of the temporal loop.

4. Convergence analysis

In this section we will prove a space-time a-priori error estimate in the energy norm (23). To this aim, we first prove the following result.

Proposition 3. *Let $\boldsymbol{w} \in \mathcal{V}_{DG}$ be the solution of (20) and let $\boldsymbol{W} \in \boldsymbol{W}_k^r$ be the solution of problem (14). Then, $|||\boldsymbol{w}||| \lesssim ||\boldsymbol{W}||_E$, provided that α in (8) is chosen large enough.*

Proof. We write $\boldsymbol{w} \in \mathcal{V}_{DG}$ as $\boldsymbol{w}(\mathbf{x}, t) = \boldsymbol{w}_1(\mathbf{x}) w_2(t)$ with $\boldsymbol{w}_1(\mathbf{x}) = \sum_{j=1}^{N_{\text{dof}}} W_j \boldsymbol{\phi}_j(\mathbf{x})$, being $\{\boldsymbol{\phi}_j\}$ a basis for $\boldsymbol{V}_h^N$ and we set $\boldsymbol{W}(t) = [W_1, \dots, W_{N_{\text{dof}}}]^T w_2(t)$. Therefore, using the definition of energy norm $|||\cdot|||$ in (10) we can write

$$\|\boldsymbol{w}(0^+)\|_{\mathcal{E}} = \|\sqrt{\rho}\dot{\boldsymbol{w}}(0^+)\|^2_{\boldsymbol{L}^2(\Omega)} + \|\sqrt{\rho}\zeta \boldsymbol{w}(0^+)\|^2_{\boldsymbol{L}^2(\Omega)} + \|\boldsymbol{w}(0^+)\|_* = T_1 + T_2 + T_3.$$

In particular T_1 reduces to

$$T_1 = \dot{w}_2(0^+)^2 \|\sqrt{\rho}\boldsymbol{w}_1\|^2_{\mathbf{L}^2(\Omega)} = \dot{w}_2(0^+)^2 \sum_{i,j=1}^{N_{\rm dof}} W_i W_j (\rho\boldsymbol{\phi}_i, \boldsymbol{\phi}_j)_\Omega$$
$$= \sum_{i,j=1}^{N_{\rm dof}} W_i \dot{w}_2(0^+) M_{ij} W_j \dot{w}_2(0^+) = (M^{1/2}\dot{\boldsymbol{W}}(0^+))^2,$$

while for T_2 and T_3 we have

$$T_2 + T_3 = \dot{w}_2(0^+)^2 \left[\|\sqrt{\rho\zeta^2}\boldsymbol{w}_1\|^2_{\mathbf{L}^2(\Omega)} + \sum_{\ell=1}^{L} \|\boldsymbol{D}^{1/2}\boldsymbol{\epsilon}(\boldsymbol{w}_1)\|^2_{\boldsymbol{\mathcal{L}}^2(\Omega_\ell)} + \|\sqrt{\eta}[\![\boldsymbol{w}_1]\!]\|^2_{\boldsymbol{\mathcal{L}}^2(\mathcal{F}_h^I)} \right]$$
$$\lesssim \dot{w}_2(0^+)^2 \left[\|\sqrt{\rho\zeta^2}\boldsymbol{w}_1\|^2_{\mathbf{L}^2(\Omega)} + \sum_{\ell=1}^{L} \|\boldsymbol{D}^{1/2}\boldsymbol{\epsilon}(\boldsymbol{w}_1)\|^2_{\boldsymbol{\mathcal{L}}^2(\Omega_\ell)} + \|\sqrt{\eta}[\![\boldsymbol{w}_1]\!]\|^2_{\boldsymbol{\mathcal{L}}^2(\mathcal{F}_h^I)} - 2(\{\boldsymbol{\sigma}(\boldsymbol{w}_1)\}, [\![\boldsymbol{w}_1]\!])_{\mathcal{F}_h^I} \right]$$
$$\lesssim \dot{w}_2(0^+)^2 \sum_{i,j=1}^{N_{\rm dof}} W_i W_j \Big[(\rho\zeta^2\boldsymbol{\phi}_i, \boldsymbol{\phi}_j)_\Omega + (\boldsymbol{\sigma}(\boldsymbol{\phi}_i), \boldsymbol{\epsilon}(\boldsymbol{\phi}_j))_\Omega + (\eta[\![\boldsymbol{\phi}_i]\!], [\![\boldsymbol{\phi}_i]\!])_{\mathcal{F}_h^I}$$
$$- (\{\boldsymbol{\sigma}(\boldsymbol{\phi}_i)\}, [\![\boldsymbol{\phi}_j]\!])_{\mathcal{F}_h^I} - ([\![\boldsymbol{\phi}_i]\!], \{\boldsymbol{\sigma}(\boldsymbol{\phi}_j)\})_{\mathcal{F}_h^I} \Big] \lesssim (E^{1/2}\boldsymbol{W}(0^+))^2.$$

where in the last step we have used α big enough. Proceeding similarly for the remaining terms in (10) we obtain

$$|||\boldsymbol{w}|||^2 \lesssim \frac{1}{2}(M^{1/2}\dot{\boldsymbol{W}}(0^+))^2 + \frac{1}{2}\sum_{n=1}^{N_T}(M^{1/2}[\dot{\boldsymbol{W}}]_n)^2 + \frac{1}{2}(M^{1/2}\dot{\boldsymbol{W}}(T^-))^2 + \sum_{n=1}^{N_T} ||C^{1/2}\dot{\boldsymbol{W}}||_{\boldsymbol{L}^2(I_n)}$$
$$+ \frac{1}{2}(E^{1/2}\boldsymbol{W}(0^+))^2 + \frac{1}{2}\sum_{n=1}^{N_T}(E^{1/2}[\boldsymbol{W}]_n)^2 + \frac{1}{2}(E^{1/2}\boldsymbol{W}(T^-))^2$$
$$= \|\boldsymbol{W}\|^2_E. \quad \square$$

We are now ready to prove the following error estimate, recalling that the numerical solution is approximated employing basis functions of degree N_ℓ (for space discretization) and basis functions of degree r_n (for time discretization).

Theorem 7. *Assume that the exact solution of problem (1) satisfies $\boldsymbol{u} \in H^2(0,T;\boldsymbol{H}^{s_\ell}(\Omega_\ell))$, $\ell = 1,\dots,L$, $s_\ell \geq 2$ and that $\boldsymbol{f} \in H^{q_n}(0,T;\boldsymbol{L}^2(\Omega))$ $\forall n = 1,\dots,N_T$. Let $\boldsymbol{u}_{DG}$ be the solution of the discrete DG formulation given in (20) with α sufficiently large. Then, it holds*

$$|||\boldsymbol{u} - \boldsymbol{u}_{DG}|||^2 \lesssim \sum_{n=1}^{N_T} \frac{k_n^{2\gamma_n - 3}}{r_n^{2q_n - 6}} \left[\|\boldsymbol{u}_h(0)\|^2_{\mathcal{E}} + \|\boldsymbol{f}\|^2_{H^{q_n}(0,T;\boldsymbol{L}^2(\Omega))} \right] + \sum_{\ell=1}^{L} \frac{h_\ell^{2\beta_\ell - 2}}{N_\ell^{2s_\ell - 3}} \|\boldsymbol{u}\|^2_{\mathbf{H}^2(0,T;H^{s_\ell}(\Omega_\ell))}$$

where $\gamma_n = \min\{r_n + 1, q_n\}$ and $\beta_\ell = \min\{N_\ell + 1, s_\ell\}$.

Proof. Supposing that $\boldsymbol{u}_h \in \boldsymbol{V}_h^N$ is the solution to the semidiscrete problem (5) we can split the error $\boldsymbol{e} = \boldsymbol{u} - \boldsymbol{u}_{DG}$ as the sum of two contributions $\boldsymbol{e}_h = \boldsymbol{u} - \boldsymbol{u}_h$ and $\boldsymbol{e}_k = \boldsymbol{u}_h - \boldsymbol{u}_{DG}$, being the former the error due to space discretization while the latter the one obtain after time integration. Then, by triangle inequality we have

$$|||\boldsymbol{u} - \boldsymbol{u}_{DG}|||^2 \leq |||\boldsymbol{e}_h|||^2 + |||\boldsymbol{e}_k|||^2.$$

We first focus on $|||\boldsymbol{e}_h|||$. Since $\boldsymbol{e}_h \in H^2(0,T;\boldsymbol{H}^2(\Omega))$, it holds $[\dot{\boldsymbol{e}}_h]_n = [\boldsymbol{e}_h]_n = 0$ $\forall n = 1,\dots,N_T$ and then $|||\boldsymbol{e}_h|||$ reduces to

$$|||\boldsymbol{e}_h|||^2 = \frac{1}{2}\|\sqrt{\rho}\dot{\boldsymbol{e}}_h(T^-)\|^2_{\mathbf{L}^2(\Omega)} + \frac{1}{2}\|\sqrt{\rho}\dot{\boldsymbol{e}}_h(0^+)\|^2_{\mathbf{L}^2(\Omega)} + \sum_{n=1}^{N_T}\|\sqrt{2\rho\zeta}\dot{\boldsymbol{e}}_h\|^2_{\mathbf{L}^2(Q_n)}$$
$$+ \frac{1}{2}\|\sqrt{\rho\zeta^2}\boldsymbol{e}_h(T^-)\|^2_{\mathbf{L}^2(\Omega)} + \frac{1}{2}\|\sqrt{\rho\zeta^2}\boldsymbol{e}_h(0^+)\|^2_{\mathbf{L}^2(\Omega)}$$
$$+ \frac{1}{2}\sum_{\ell=1}^{L}\|\boldsymbol{D}^{1/2}\boldsymbol{\epsilon}(\boldsymbol{e}_h(T^-))\|^2_{\boldsymbol{\mathcal{L}}^2(\Omega_\ell)} + \frac{1}{2}\sum_{\ell=1}^{L}\|\boldsymbol{D}^{1/2}\boldsymbol{\epsilon}(\boldsymbol{e}_h(0^+))\|^2_{\boldsymbol{\mathcal{L}}^2(\Omega_\ell)}$$
$$+ \frac{1}{2}||\sqrt{\eta}[\![\boldsymbol{e}_h(T^-)]\!]||^2_{\boldsymbol{\mathcal{L}}^2(\mathcal{F}_h^I)} + \frac{1}{2}||\sqrt{\eta}[\![\boldsymbol{e}_h(0^+)]\!]\|^2_{\boldsymbol{\mathcal{L}}^2(\mathcal{F}_h^I)}.$$

By using the classical trace inequality, cf. [52], we get

$$
\begin{aligned}
|||\boldsymbol{e}_h|||^2 \lesssim & \int_0^T \left[\|\sqrt{\rho}\dot{\boldsymbol{e}}_h\|^2_{\mathbf{L}^2(\Omega)} + \|\sqrt{\rho\zeta^2}\boldsymbol{e}_h\|^2_{\mathbf{L}^2(\Omega)} + \sum_{\ell=1}^{L} \|\boldsymbol{D}^{1/2}\boldsymbol{\epsilon}(\boldsymbol{e}_h)\|^2_{\mathcal{L}^2(\Omega_\ell)} + \|\sqrt{\eta}[\![\boldsymbol{e}_h]\!]\|^2_{\mathcal{L}^2(\mathcal{L}_h^I)} \right] + \\
& + \int_0^T \left[\|\sqrt{\rho}\ddot{\boldsymbol{e}}_h\|^2_{\mathbf{L}^2(\Omega)} + \|\sqrt{\rho\zeta^2}\dot{\boldsymbol{e}}_h\|^2_{\mathbf{L}^2(\Omega)} + \sum_{\ell=1}^{L} \|\boldsymbol{D}^{1/2}\boldsymbol{\epsilon}(\dot{\boldsymbol{e}}_h)\|^2_{\mathcal{L}^2(\Omega_\ell)} + \|\sqrt{\eta}[\![\dot{\boldsymbol{e}}_h]\!]\|^2_{\mathcal{L}^2(\mathcal{F}_h^I)} \right] = \\
& = \int_0^T \|\boldsymbol{e}_h\|^2_{\mathcal{E}} + \int_0^T \|\dot{\boldsymbol{e}}_h\|^2_{\mathcal{E}}.
\end{aligned}
$$

We next use the result of Theorem 2 so that

$$
\begin{aligned}
\int_0^T \|\boldsymbol{e}_h\|^2_{\mathcal{E}} &\lesssim \sum_{\ell=1}^{L} \frac{{h_\ell}^{2\beta_\ell-2}}{N_\ell^{2s_\ell-3}} \left(\int_0^T \mathcal{I}(\boldsymbol{u})(t)\,dt + T\int_0^T \mathcal{I}(\dot{\boldsymbol{u}})(t)\,dt \right) \\
\int_0^T \|\dot{\boldsymbol{e}}_h\|^2_{\mathcal{E}} &\lesssim \sum_{\ell=1}^{L} \frac{{h_\ell}^{2\beta_\ell-2}}{N_\ell^{2s_\ell-3}} \left(\int_0^T \mathcal{I}(\dot{\boldsymbol{u}})(t)\,dt \right),
\end{aligned}
$$

with $\beta_\ell = \min\{s_\ell, N_\ell + 1\}$, for all $\ell = 1, ..., L$ and the following inequalities

$$
\begin{aligned}
\int_0^T \mathcal{I}(\boldsymbol{u})(t)\,dt &= \int_0^T \left(\|\dot{\boldsymbol{u}}(t)\|^2_{\mathbf{H}^{s_\ell}(\Omega_\ell)} + \|\boldsymbol{u}(t)\|^2_{\mathbf{H}^{s_\ell}(\Omega_\ell)} \right) dt \le \|\boldsymbol{u}\|^2_{H^2(0,T;\boldsymbol{H}^{s_\ell}(\Omega_\ell))} \\
\int_0^T \mathcal{I}(\dot{\boldsymbol{u}})(t)\,dt &= \int_0^T \left(\|\ddot{\boldsymbol{u}}(t)\|^2_{\mathbf{H}^{s_\ell}(\Omega_\ell)} + \|\dot{\boldsymbol{u}}(t)\|^2_{\mathbf{H}^{s_\ell}(\Omega_\ell)} \right) dt \le \|\boldsymbol{u}\|^2_{H^2(0,T;\boldsymbol{H}^{s_\ell}(\Omega_\ell))},
\end{aligned}
$$

to obtain

$$
|||\boldsymbol{e}_h|||^2 \lesssim \sum_{\ell=1}^{L} \frac{h_\ell^{2\beta_\ell-2}}{N_\ell^{2s_\ell-3}} \|\boldsymbol{u}\|^2_{H^2(0,T;\mathbf{H}^{s_\ell}(\Omega_\ell))}. \tag{31}
$$

Now we estimate $|||\boldsymbol{e}_k|||$. By using the result in Proposition 3 and Theorem 4 we obtain

$$
\begin{aligned}
|||\boldsymbol{e}_k||| \lesssim \|\boldsymbol{E}_k\|_E^2 &\lesssim \sum_{n=1}^{N_T} \frac{k_n^{2\beta_n-3}}{r_n^{2q_n-6}} \|\boldsymbol{u}_h\|^2_{\mathbf{H}^{q_n}(I_n)} \\
&\lesssim \sum_{n=1}^{N_T} \frac{k_n^{2\beta_n-3}}{r_n^{2q_n-6}} \int_{I_n} \left(\|\boldsymbol{u}_h(t)\|^2_{\mathbf{L}^2(\Omega)} + \|\dot{\boldsymbol{u}}_h(t)\|^2_{\mathbf{L}^2(\Omega)} + \cdots + \|\boldsymbol{u}_h^{(q_n)}(t)\|^2_{\mathbf{L}^2(\Omega)} \right) dt,
\end{aligned}
$$

where $\beta_n = \min\{r_n + 1, q_n\}$, for any $n = 1, \ldots, N_T$. Finally, using the result of Theorem 1 we get

$$
\int_{I_n} \|\boldsymbol{u}_h(t)\|^2_{\mathbf{L}^2(\Omega)}\,dt \lesssim \int_{I_n} \|\boldsymbol{u}_h(t)\|^2_{\mathcal{E}}\,dt \lesssim T \left(\|\boldsymbol{u}_h(0)\|^2_{\mathcal{E}} + \int_0^T \|\boldsymbol{f}(\tau)\|^2_{\mathbf{L}^2(\Omega)}\,d\tau \right),
$$

and

$$
\int_{I_n} \|\boldsymbol{u}_h^{(q_n)}\|^2_{\mathbf{L}^2(\Omega)} \lesssim \int_{I_n} \|\boldsymbol{u}_h^{(q_n)}\|^2_{\mathcal{E}} \lesssim T \left(\int_0^T \|\boldsymbol{f}^{(q_n)}(\tau)\|^2_{\mathbf{L}^2(\Omega)}\,d\tau \right).
$$

Then

$$
|||\boldsymbol{e}_k|||^2 \lesssim \sum_{n=1}^{N_T} \frac{k_n^{2\beta_n-3}}{r_n^{2q_n-6}} \left(\|\boldsymbol{u}_h(0)\|^2_{\mathcal{E}} + \|\boldsymbol{f}\|^2_{H^{q_n}(0,T;\boldsymbol{L}^2(\Omega))} \right), \tag{32}
$$

with $\beta_n = \min\{r_n + 1, q_n\}$. Putting together estimate (31) and (32) we obtain the thesis. □

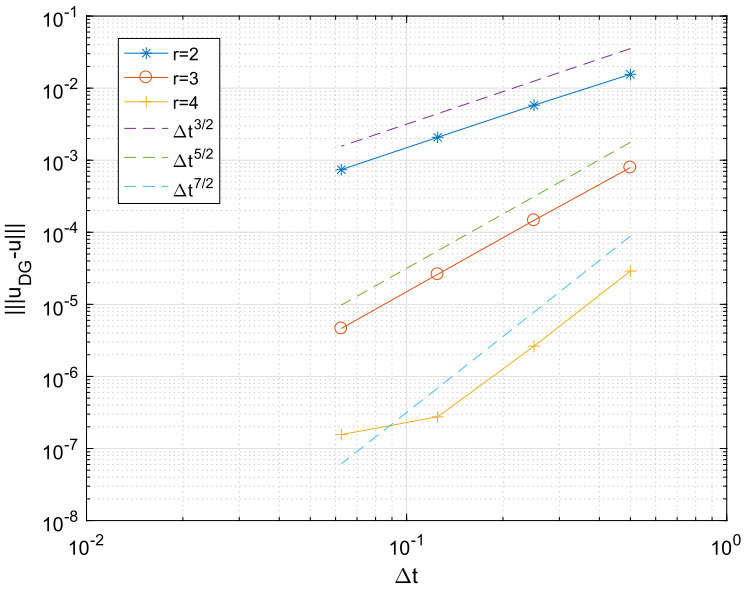

Fig. 4. Computed errors $|||\boldsymbol{e}||| = |||\boldsymbol{u}_{DG} - \boldsymbol{u}|||$ as a function of time-step Δt, with $r = 2, 3, 4$, $h = 0.1$ and $N = 8$. (For interpretation of the colors in the figure(s), the reader is referred to the web version of this article.)

Corollary 4.1. *Under the same assumption of Theorem 7, suppose moreover that the solution to problem (1) is regular enough with* $s_\ell = s\ \forall \ell = 1, \dots, L$ *and* $q_n = q\ \forall n = 1, \dots, N_T$. *If we set* $h_\ell = h$, $N_\ell = N\ \forall \ell = 1, \dots, L$ *and* $k_n = k$, $r_\ell = r\ \forall n = 1, \dots, N_T$, *then it holds*

$$|||\boldsymbol{u} - \boldsymbol{u}_{DG}||| \lesssim \frac{k^{\gamma-3/2}}{r^{q-3}} \left[\|\boldsymbol{u}_h(0)\|_{\mathcal{E}} + \|\boldsymbol{f}\|_{H^q(0,T;\boldsymbol{L}(\Omega))} \right] + \frac{h^{\beta-1}}{N^{s-3/2}} \|\boldsymbol{u}\|^2_{\mathbf{H}^2(0,T;H^s(\Omega_\ell))}, \tag{33}$$

where $\gamma = \min\{r+1, q\}$ *and* $\beta = \min\{N+1, s\}$.

5. Numerical results

In this section we present a set of numerical experiments on both two and three dimensions aiming, on one side, to verify the theoretical bounds presented in the previous sections and, on the other side, to apply our numerical method to realistic applications. The numerical results have been obtained through a Matlab program, for 2D problems, while through a suitable modification of the open-source software SPEED (http://speed.mox.polimi.it/), for 3D problems, see [46].

5.1. Verification tests

5.1.1. Two-dimensional test case

We set $I = (0, T]$, $T = 1$, and $\Omega = (0, 1)^2$ with homogeneous Dirichlet boundary conditions, i.e. $\Gamma_N = 0$, $\Gamma_D = \partial\Omega$. We take the external force $\boldsymbol{f}$ and the initial conditions $\boldsymbol{u}_0$, $\boldsymbol{u}_1$ so that the exact solution of (1) is

$$\boldsymbol{u}(t) = e^{-t} \begin{bmatrix} \sin(\pi x)^2 \sin(2\pi y) \\ \sin(2\pi x) \sin(\pi y)^2 \end{bmatrix}, \quad t \in [0, T]. \tag{34}$$

On the one hand, we consider a decomposition $\mathcal{T}_h$ of Ω made by a single macro element, i.e. $\Omega = \Omega_1$, we introduce a conforming Cartesian mesh of granularity h in Ω_1, and choose a polynomial degree $N_1 = N \geq 2$ for the spatial discretization. On the other hand, we use a uniform time domain partition of step size Δt and set a uniform polynomial degree $r \geq 2$ for the temporal discretization. We compute the error $|||\boldsymbol{u}_{DG} - \boldsymbol{u}|||$ by employing the energy norm (23), and verify the error estimate (33) separately in space and time. We firstly set $h = 0.1$ corresponding to 100 elements and fix $N = 8$, and let the time step Δt varying from 0.5 to 0.0625 for $r = 2, 3, 4$. The computed energy errors are shown in Fig. 4 and are in agreement with the theoretical results, cf. Theorem 7.

Now, we fix the time step $\Delta t = 0.01$, the polynomial degree $r = 6$ and we use increasingly refined spatial grids with $h = 0.5, 0.25, 0.125, 0.0625$, for different choices of the polynomial degree $N = 2, 3, 4$. The results are shown in Fig. 5. We observe that there is a perfect correspondence between the numerical results and the theoretical error estimates predicted by Corollary 4.1.

Finally, we fix a grid size $h = 0.125$, a time step $\Delta t = 0.01$ and make vary together the polynomial degrees, $N = r = 2, 3, 4, 5$. Fig. 6 shows that the computed error decays as expected from (33).

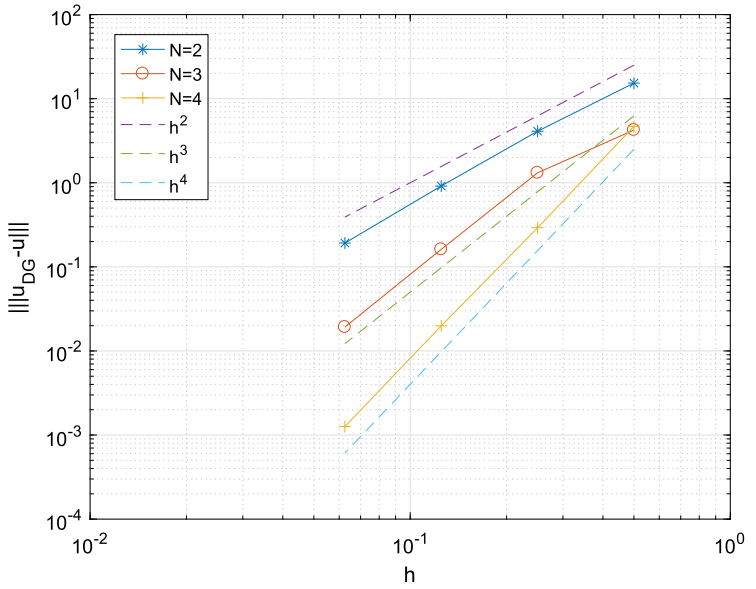

Fig. 5. Computed errors $|||\boldsymbol{e}||| = |||\boldsymbol{u}_{DG} - \boldsymbol{u}|||$ as a function of mesh size h, with $N = 2, 3, 4$, $\Delta t = 0.01$ and $r = 6$.

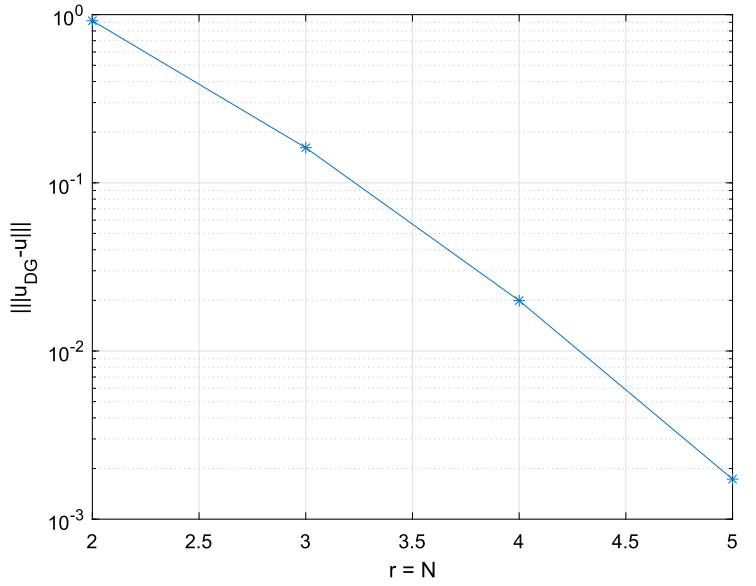

Fig. 6. Computed errors $|||\boldsymbol{e}||| = |||\boldsymbol{u}_{DG} - \boldsymbol{u}|||$ as a function of polynomial degree $N = r$, with $\Delta t = 0.1$, $h = 0.25$.

5.1.2. Three-dimensional test case

We set $I = (0, T]$, $T = 10$, and $\Omega = (0, 1)^3$ with homogeneous Dirichlet boundary conditions, i.e. $\Gamma_N = 0$, $\Gamma_D = \partial\Omega$. We fix the external force $\boldsymbol{f}$ and the initial conditions $\boldsymbol{u}_0$, $\boldsymbol{u}_1$ so that the exact solution of (1) is

$$\boldsymbol{u}(t) = \cos(3\pi t) \begin{bmatrix} \sin(\pi x)^2 \sin(2\pi y) \sin(2\pi z) \\ \sin(2\pi x) \sin(\pi y)^2 \sin(2\pi z) \\ \sin(2\pi x) \sin(2\pi y) \sin(\pi z)^2 \end{bmatrix}, \quad t \in [0, T]. \tag{35}$$

We proceed analogously to the two-dimensional case. We set a single macro element $\Omega = \Omega_1$, partitioned into a conforming hexahedral mesh of granularity h, and we use a uniform time domain partition of step size Δt. We choose polynomial degree $N_1 = N \geq 2$ for the space discretization and degree $r \geq 2$ for the temporal one. We firstly set $h = 0.0125$ corresponding to 512 elements and fix $N = 4$, and let the time step Δt varying from 0.4 to 0.00625 for $r = 2, 3, 4$. The computed energy errors are shown in Fig. 7. We can observe that the numerical results are in agreement with the theoretical ones. We

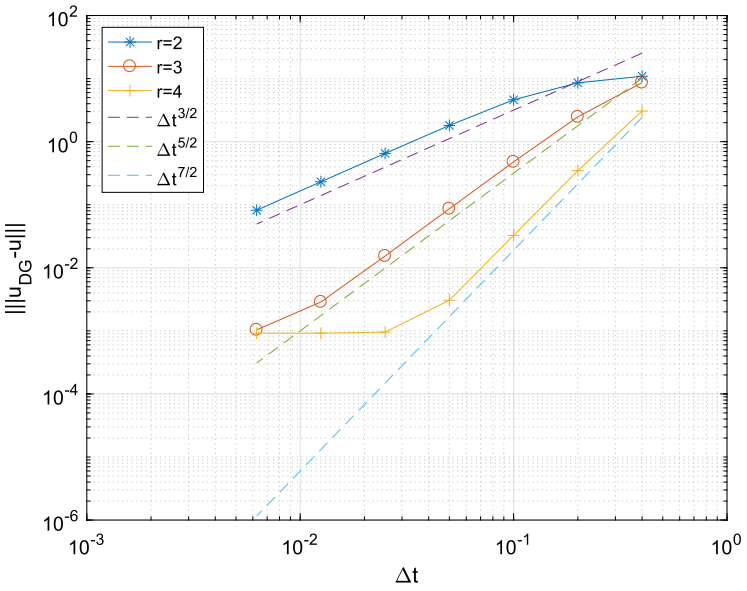

Fig. 7. Computed errors $|||\boldsymbol{e}||| = |||\boldsymbol{u}_{DG} - \boldsymbol{u}|||$ as a function of time-step Δt, with $r = 2, 3, 4$, $h = 0.125$ and $N = 4$.

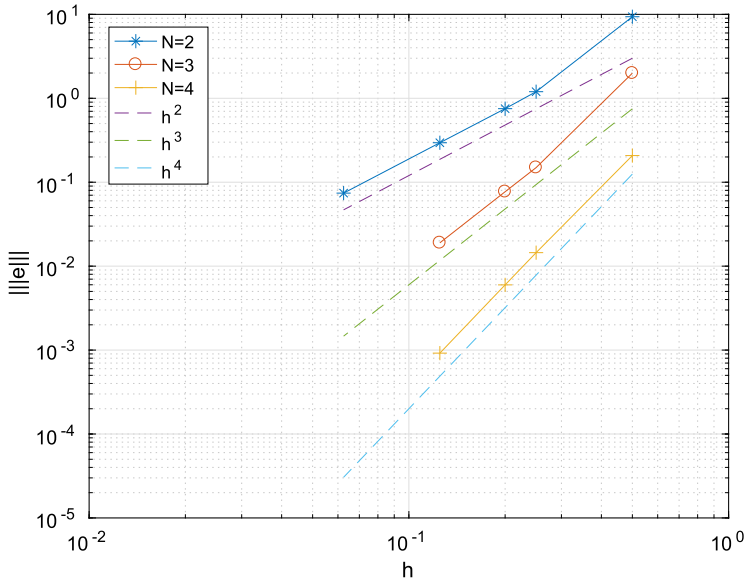

Fig. 8. Computed errors $|||\boldsymbol{e}||| = |||\boldsymbol{u}_{DG} - \boldsymbol{u}|||$ as a function of mesh size h, with $N = 2, 3, 4$, $\Delta t = 0.001$ and $r = 5$.

note that with $r = 4$, the error reaches a plateau for $\Delta t \leq 0.025$. However, this effect could be easily overcome by increasing the spatial polynomial degree N and/or by refining the mesh size h.

Then, we fix the time step $\Delta t = 0.001$, the polynomial degree $r = 5$ and we use increasingly refined spatial grids with $h = 0.5, 0.25, 0.2, 0.125, 0.0625$, for different choices of the polynomial degree $N = 2, 3, 4$. The results are shown in Fig. 8 and are in a perfect correspondence with the theoretical error estimates predicted by Corollary 4.1.

Finally we fix a grid size $h = 0.25$, a time step $\Delta t = 0.1$ and let vary together the polynomial degrees, $N = r = 2, 3, 4, 5$. Fig. 9 shows the decay of the error, that is again in agreement with (33).

Moreover, in Table 1 and 2 we report the energy $|||\boldsymbol{u} - \boldsymbol{u}_{DG}|||$ and the $\|\boldsymbol{u} - \boldsymbol{u}_{DG}\|_{\mathbf{L}^2(\Omega\times(0,T])}$-norms evaluated at the final observation time T. Here we make vary simultaneously the time-step and the mesh size. We consider the case $N = r = 2$ in Table 1 and $N = r = 3$ in Table 2. Similar conclusions as the ones stated before can be drawn.

To complete the analysis, in Fig. 10 we investigate the behavior of our method in terms of energy conservation, plotting the space energy norm of the approximated solution (10) as a function of time. We solve problem (1) setting $\zeta = 0$ and $\boldsymbol{f} = 0$, i.e. without damping and external forces. The initial conditions are the same as before.

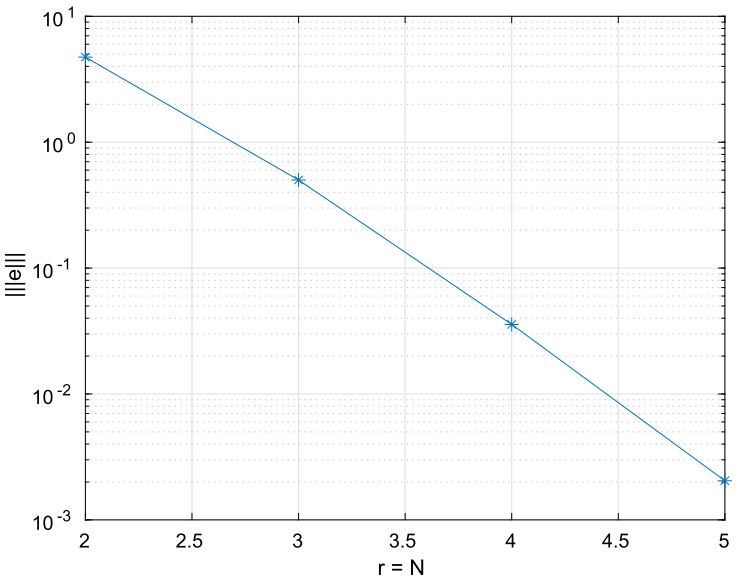

Fig. 9. Computed errors $|||\boldsymbol{e}||| = |||\boldsymbol{u}_{DG} - \boldsymbol{u}|||$ as a function of polynomial degree $N = r$, with $\Delta t = 0.1$, $h = 0.25$.

Table 1
Energy (left) and L^2-norm (right) of the error computed employing polynomial degree $N = r = 2$.

$\|\|\|\boldsymbol{u} - \boldsymbol{u}_{DG}\|\|\|$				
$h\|\Delta t$	0.5	0.25	0.125	0.0625
0.5	11.97	13.81	10.14	9.44
0.25	10.32	9.18	6.01	2.74
0.125	10.16	9.19	5.93	2.50
0.0625	10.15	9.20	5.93	2.49

$\|\boldsymbol{u} - \boldsymbol{u}_{DG}\|_{L^2(\Omega\times(0,T))}$				
$h\|\Delta t$	0.5	0.25	0.125	0.0625
0.5	0.6583	0.5784	0.6856	0.8490
0.25	0.5238	0.4936	0.2332	0.0454
0.125	0.5238	0.4936	0.2330	0.0431
0.0625	0.5238	0.4936	0.2331	0.0429

Table 2
Energy (left) and L^2-norm (right) of the error computed employing polynomial degree $N = r = 3$.

$\|\|\|\boldsymbol{u} - \boldsymbol{u}_{DG}\|\|\|$				
$h\|\Delta t$	0.5	0.25	0.125	0.0625
1	15.21	8.85	8.08	8.05
0.5	9.64	4.00	2.12	1.99
0.25	9.89	3.98	0.83	0.21
0.125	9.89	3.98	0.82	0.15

$\|\boldsymbol{u} - \boldsymbol{u}_{DG}\|_{L^2(\Omega\times(0,T))}$				
$h\|\Delta t$	0.5	0.25	0.125	0.0625
1	0.5688	0.3364	0.3529	0.3537
0.5	0.5095	0.1511	0.1036	0.1012
0.25	0.5234	0.1014	0.0046	0.0008
0.125	0.5233	0.1016	0.0047	0.0002

In accordance to estimate (26), we can conclude that the proposed method is dissipative. However, the dissipation error can be effectively reduced by properly choosing the discretization parameters, cf. Fig. 10.

5.2. Geophysical applications

5.2.1. Visco-elastic waves in a semi-infinite medium

This test case (taken from [47, Section 3.6.3]) addresses a wave propagation problem in a semi-infinite medium originated by an impulsive load applied to the domain's surface. We consider the computational domain $\Omega = (0, 0)$ m $\times (1, 0.5)$ m, apply first order absorbing boundary conditions [43,54] at bottom, right and left sides of the domain and impose a Neumann's condition on the top surface, see Fig. 11. The impulse load $\boldsymbol{g}_N = \boldsymbol{\sigma}(\boldsymbol{u})\boldsymbol{n}$ applied at the top surface is given by

$$\boldsymbol{g}_N(x, y, t) = \begin{cases} (0, -30)\ \mathrm{N/m^2} & \text{if } x \in [0.375, 0.425] \cup [0.575, 0.625],\ y = 0.5,\ t \le 0.005, \\ (0, 0)\ \mathrm{N/m^2} & \text{otherwise.} \end{cases}$$

The medium is homogeneous with material parameters $\rho = 1$ kg/m^3, $\mu = 1$ kN/m^2, $\lambda = 2$ kN/m^2 and damping factor $\zeta = 1$ s^{-1}. Null conditions are imposed for the initial displacement and velocity, i.e., $\boldsymbol{u}(0) = \partial_t \boldsymbol{u}(0) = \boldsymbol{0}$.

In Fig. 12 we report the magnitude of the displacement computed at different times by fixing the polynomial degree in space and time equal to 3, i.e. $N = r = 3$, and choosing a time step $\Delta t = 0.005$ *s*. The solution is in agreement with the one shown in [47]. Indeed, we notice two wavefronts that propagate downwards with different velocities corresponding to

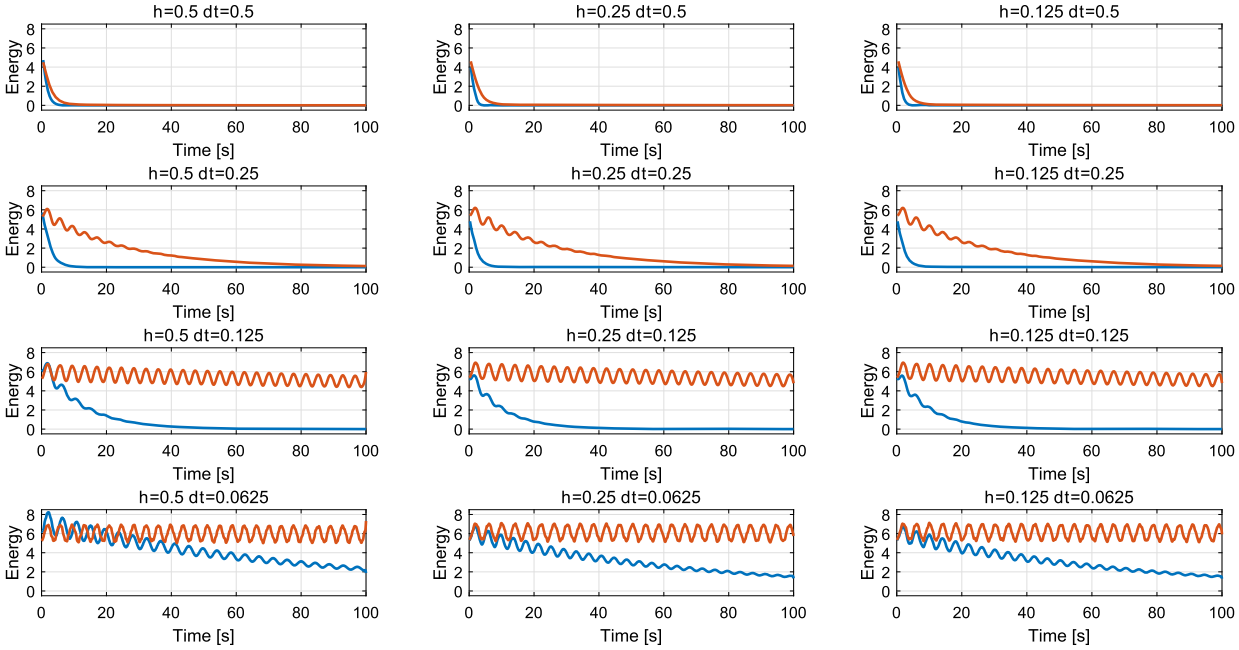

Fig. 10. Computed space energy (10) of the numerical solution $\boldsymbol{u}_{DG}$ obtained with $N = r = 2$ (blue) and $N = r = 3$ (red).

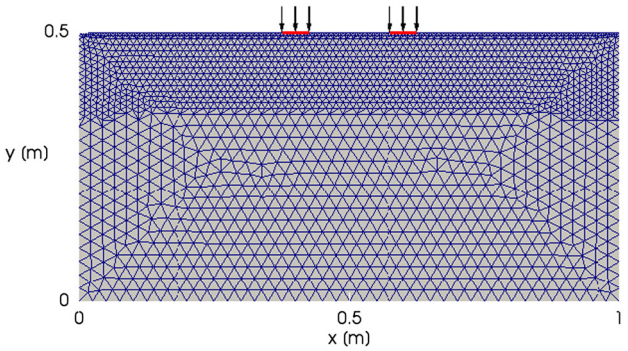

Fig. 11. Geometry and spatial grid for test case of Section 5.2.1.

pressure and shear waves. Moreover surface waves propagate with smaller velocity and with smaller attenuation leftwards and rightwards.

5.2.2. Dynamic load test

Similarly to the previous test case, we study in a homogeneous domain the wave propagation induced by a dynamic load applied to the domain's boundary. This analysis is similar to the one shown in [53, Section 6.3] and goes under the name of dynamic load plate test (DLPT). The purpose of the DLPT is the study of the soil deflection due to a falling weight impacting a rigid disk in contact with the soil surface. DPLT is a non-destructive technique used in geomechanics for a quick assessment of the field compaction quality [2,57]. Here, we neglect the soil-plate interaction, and consider a stress pulse applied directly to the soil surface as it is described in the following.

We set $\Omega = (-5, 5)\ \mathrm{m} \times (0, 3)\ \mathrm{m}$ and assign homogeneous Dirichlet boundary conditions on the bottom and lateral edges while a stress load condition is applied on the top edge as follows:

$$\boldsymbol{g}_N(x, y, t) = \begin{cases} (0, -\frac{10^5}{2} \sin(50\pi t))\ \mathrm{N/m^2} & \text{if } x \in [-0.15, 0.15] \text{ and } t \leq 0.02\ \mathrm{s}, \\ (0, 0)\ \mathrm{N/m^2} & \text{otherwise}, \end{cases}$$

where $\boldsymbol{g}_N = \boldsymbol{\sigma}(\boldsymbol{u})\boldsymbol{n}$, cf. Fig. 13. Null initial conditions have been set for the displacement and the velocity field. For the following analysis we account for two different sets of material properties, summarized in Table 3.

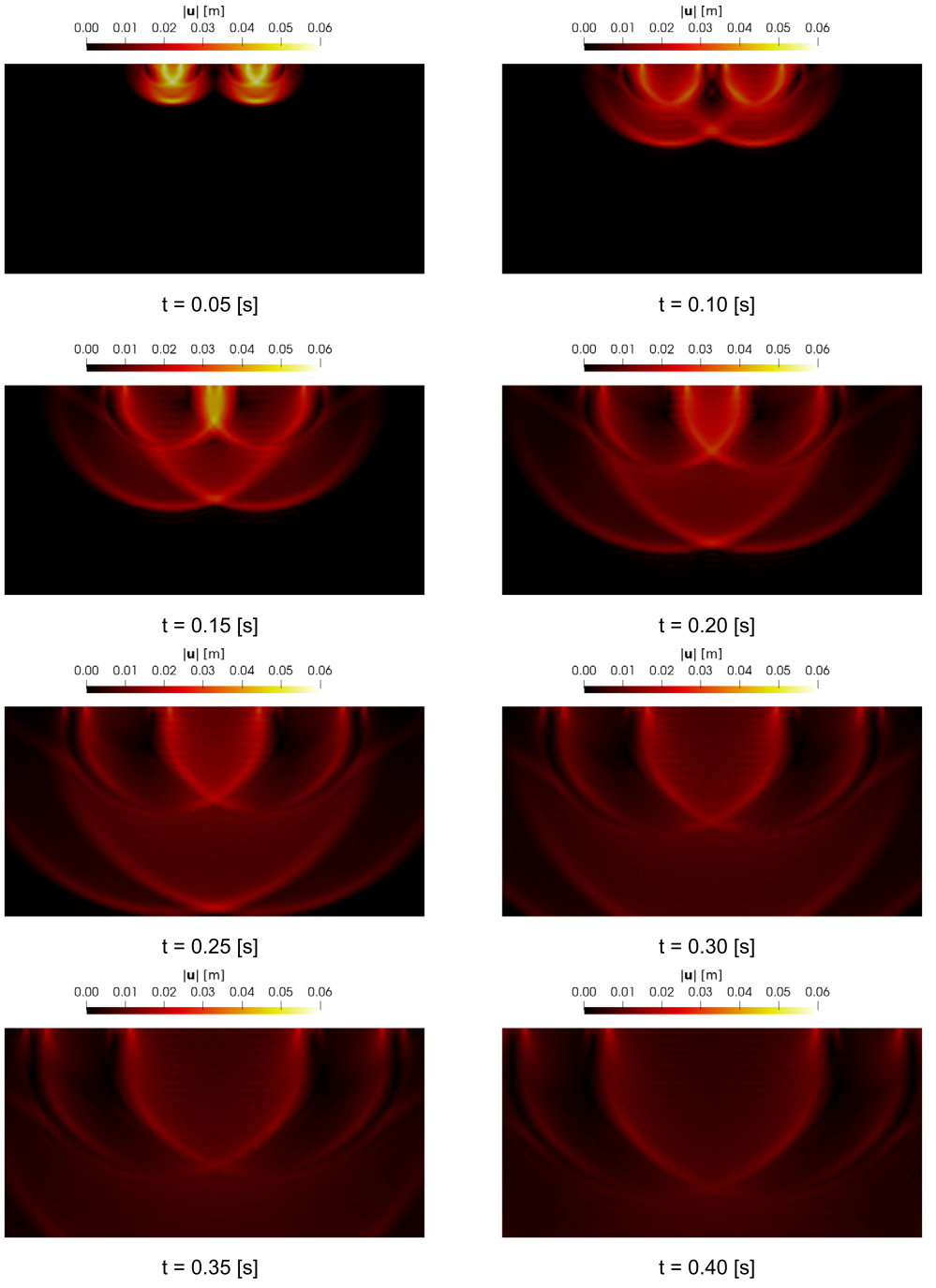

Fig. 12. Solution of test case of Section 5.2.1. Magnitude of the displacement at different times obtained with uniform time-step $\Delta t = 0.005$ s and a space-time polynomial degree $N = r = 3$.

We consider one space subdomain, i.e. $L = 1$, having a mesh size varying from 0.01 m to 0.36 m, cf. Fig. 13, and set a uniform space polynomial degree $N = 3$. Moreover, we consider uniform time-slabs of size $\Delta t = 0.002$ s with a time polynomial degree $r = 3$.

In Fig. 14, we report the evolution of the vertical component of the displacement at four points located on the top surface, while in Fig. 15 we show a snapshot of the vertical displacement computed at time $t = 0.014$ s for both sets of parameters. Because of the different hypothesis on the data set of the model, our numerical results present some differences compared to the ones in [53]. In particular, the time location of the maximum vertical displacement is a bit delayed and its

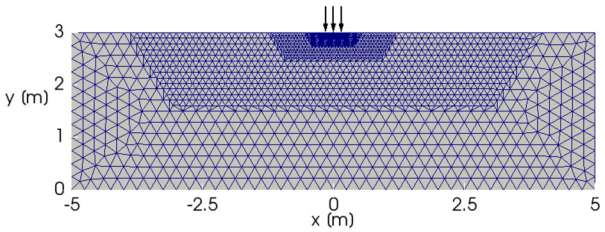

Fig. 13. Geometry and spatial grid for test case of Section 5.2.2.

Table 3
Material properties of test case of Section 5.2.2. Here, the Lamé parameters λ and μ can be obtained through the relations $\mu = \rho c_s^2$ and $\lambda = \rho c_p^2 - \mu$.

	Set 1	Set 2
ρ [kg/m^3]	2000	2000
c_p [m/s]	81.204	115.791
c_s [m/s]	134.388	191.532
ζ [1/s]	0.01	0.01

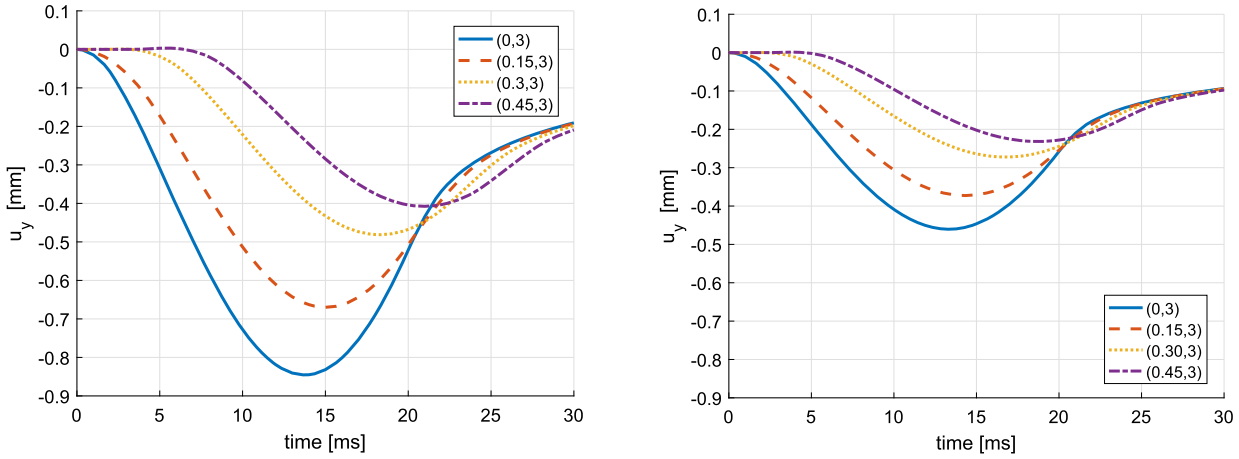

Fig. 14. Solution of test case of Section 5.2.2. Time evolution of the second component of the displacement at four points located on the top surface obtained with Set 1 (left) and Set 2 (right) of parameters.

amplitude is a little bit larger. However the result are comparable. In addition we remark that, as expected, larger values of the vertical displacement are obtained with a softer soil, i.e., with mechanical properties of Set 1.

5.2.3. Wave propagation in heterogeneous media

The following experiment aims at testing our method on a complex geometry. Therefore, we simulate the propagation of seismic wave in an idealized bidimensional Earth's cross section. The computational domain $\Omega = (0, 38.4)$ km $\times$ $(0, 10)$ km is composed by 7 different material layers and is represented in Fig. 16 along with the mesh grid. We set a free surface condition on top of the domain, i.e., $\boldsymbol{\sigma}(\boldsymbol{u})\boldsymbol{n} = \mathbf{0}$, while we impose homogeneous Dirichlet boundary conditions elsewhere. We simulate a point source load of the form

$$\boldsymbol{f}(\mathbf{x}, t) = \left(0, Ae^{-10^{-4}\|\mathbf{x}-\mathbf{x}_s\|^2}(1-2\pi^2)f_0^2(t-t_0)^2e^{-\pi^2 f_0^2(t-t_0)^2}\right),$$

with $A = 10^3$ N, $f_0 = 2$ Hz and $t_0 = 2$ s applied at the point $\mathbf{x}_s = (19.4, 7.8)$ km. Material properties are assigned according to Table 4.

The computational domain (see Fig. 16) is discretized using an unstructured grid consisting of 7547 triangular elements, with a variable mesh size ranging from 230 m for Layer 1 to 900 m for Layer 7. We employ a uniform space polynomial degree $N_\ell = N = 3$, for $\ell = 1, \ldots, 7$. We partition the time domain into uniform time-slabs of amplitude $\Delta t = 0.1$ s and chose a time polynomial degree $r_n = r = 3$ for all the slabs. We remark that the discretization parameters are chosen is order to guarantee a good representation of the wave field according to the convergence results shown in the previous section.

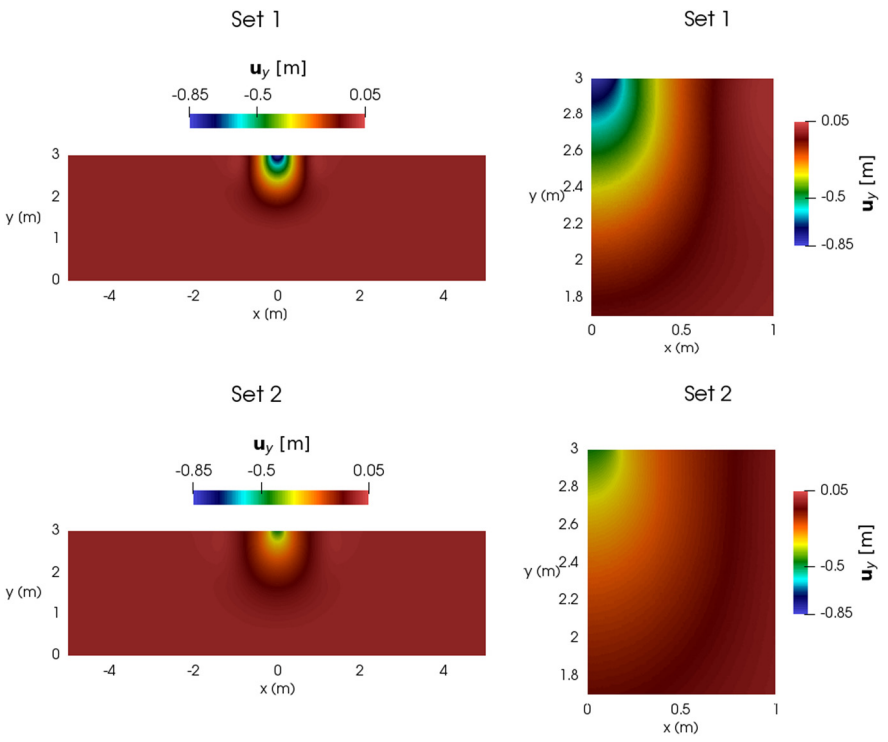

Fig. 15. Computed vertical displacement for test case of Section 5.2.2 at time $t = 0.014$ s for Set 1 (top) and Set 2 (bottom).

Table 4
Material properties of test case of Section 5.2.3. Here, the Lamé parameters λ and μ can be obtained through the relations $\mu = \rho c_s^2$ and $\lambda = \rho c_p^2 - \mu$.

Layer Ω_ℓ	ρ [kg/m^3]	c_p [m/s]	c_s [m/s]	ζ [1/s]
1	1800	1321	294	0.0680
2	1800	2024	450	0.0444
3	2050	1920	600	0.0333
4	2050	1920	650	0.0308
5	2050	2000	650	0.0308
6	2400	3030	1515	0.0320
7	2450	3200	1600	0.0125

The computed displacement wave field $\boldsymbol{u}_{DG} = (\boldsymbol{u}_x, \boldsymbol{u}_y)$ is shown in Fig. 17 for different time instants. We notice that the heterogeneity of the soil produce oscillations and perturbations on the wave front. In particular, due to the stratigraphy of the model, the energy is mainly focused towards the left of the domain, reaches the surface of the model and (most of it) remains trapped within the first layer. All these complex and relevant phenomena are well captured by the proposed method and are in agreement with the ones shown in [9]. Finally, we observe a reflexion of the wavefront coming from the bottom surface due to the presence of a Dirichlet condition.

5.2.4. Plane wave propagation

The last experiment is aimed at comparing the performance of our method with a DGSE space discretization coupled with leap-frog time integration scheme for the solution of (1).

We consider a plane wave propagating along the vertical direction in a (horizontally stratified) heterogeneous domain having dimensions $\Omega = (0, 100)$ m $\times$ $(0, 100)$ m $\times$ $(-1850, 0)$ m, cf. Fig. 18 and Table 5. The source plane wave is polarized in the x direction and its time dependency is given by a unit amplitude Ricker wave with peak frequency at 2 Hz. The subdomains are discretized in space with a cartesian hexahedral grid having size h ranging from 15 m in the top layer to 50 m in the bottom layer. We impose a free surface condition on the top surface, absorbing boundary conditions on the bottom surface and homogeneous Dirichlet conditions along the y and z direction on the remaining boundaries.

In Fig. 19 (left) we report the computed time history of the first component of the displacement field, namely $\boldsymbol{u}_x$, on a receiver located at (50 m, 50 m, 0 m) on the free surface. We compare the results obtained with the space-time dG method (with $N_\ell = N = 2$ $\forall \ell$, $r_n = r = 2$ $\forall n$ and $\Delta t = 10^{-2}$ s) and the DGSE method coupled with the leap-frog scheme (with $N = 2$ and $\Delta t = 10^{-4}$) with a reference semi-analytical solution $\boldsymbol{u}_{TH}$ obtained with the Thomson-Haskell propagation

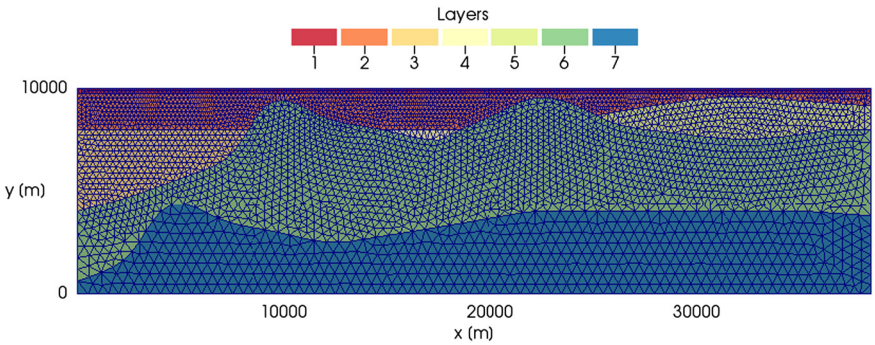

Fig. 16. Geometry and spatial grid of test case of Section 5.2.3.

Table 5
Mechanical properties for test case of Section 5.2.4. Here, the Lamé parameters λ and μ can be obtained through the relations $\mu = \rho c_s^2$ and $\lambda = \rho c_p^2 - \mu$.

Layer	Height [m]	ρ [kg/m^3]	c_p [m/s]	c_s [m/s]	ζ [1/s]
Ω_1	15	1800	1064	236	0.261
Ω_2	15	1800	1321	294	0.216
Ω_3	20	1800	1494	332	0.190
Ω_4	30	1800	1664	370	0.169
Ω_5	40	1800	1838	408	0.153
Ω_6	60	1800	2024	450	0.139
Ω_7	120	2050	1988	523	0.120
Ω_8	500	2050	1920	600	0.105
Ω_9	400	2400	3030	1515	0.041
Ω_{10}	600	2400	4180	2090	0.030
Ω_{11}	50	2450	5100	2850	0.020

Table 6
Comparison of the performance for the resolution of test case of Section 5.2.4. Total execution time of the DGSE method coupled with the leap-frog scheme versus the space-time dG method. The accuracy of the methods is compared using the ℓ^2-norm of the error in the x component of the displacement $\boldsymbol{u}_x$, computed using the semi-analytic solution.

$N = r$	Leap-frog			Time-DG				
	Δt	Exec. time	*error*	Δt	nnz(A)	Mat. build	Time loop	*error*
2	10^{-4}	180 s	0.065	10^{-1}	$8.6 \cdot 10^8$	39 s	31 s	0.104
2	10^{-4}	180 s	0.065	10^{-2}	$8.6 \cdot 10^8$	39 s	171 s	0.065

matrix method, [33]. As one can see the three different curves overlap each others and are in a good qualitative agreement. To have a quantitative measure of the misfits with respect to the semi analytical solution we report in Fig. 19 (right) the time evolution of the error $e_x = |\boldsymbol{u}_{DG,x} - \boldsymbol{u}_{TH,x}|$. We notice that both numerical methods achieve the same level of accuracy. Finally, in Table 6, we compare the efficiency of the schemes here denoted as "time to solution". From the second row in Table 6 we can conclude that the space-time dG scheme is as good as the leap-frog time integration. However, due to the assembly phase of the linear system in (30) it becomes much more expensive (third row in Table 6). In addition, if one employs a direct solver, this reveals to be a great limitation concerning the dimension of the problems that we can consider due to the amount of memory required to store the entries of the matrix. In this situation, a suitable iterative algorithm is preferable. This will be a topic for a future research.

6. Conclusions

In this work we have presented a space-time Discontinuous Galerkin method for the numerical approximation of visco-elastic wave propagation problems. We have built an energy norm that naturally arose by the variational formulation of the problem, and that we have employed to prove well-posedness, stability and error bounds. We have implemented our method either in Matlab and in the open-source software SPEED and we have verified and validated the proposed numerical algorithm on some two and three dimensional benchmarks.

Fig. 17. Computed displacement wave field for test case of Section 5.2.3 at different time instants obtained with a uniform time-step $\Delta t = 0.1$ s and a space-time polynomial degree $N = r = 3$.

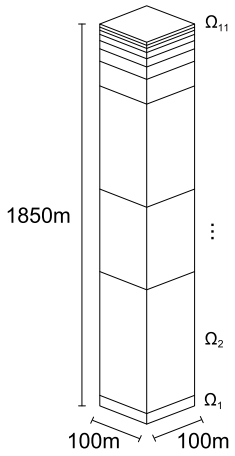

Fig. 18. Computational domain $\Omega = \cup_{\ell=1}^{11} \Omega_\ell$ of test case of Section 5.2.4.

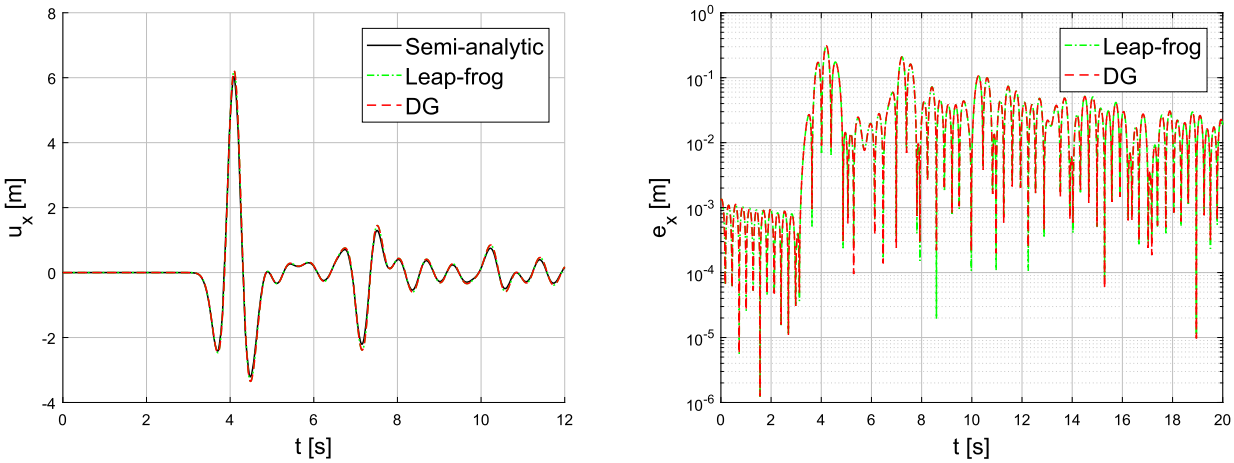

Fig. 19. Solution of test case of Section 5.2.4. Left: time evolution of the first component of the displacement field $\boldsymbol{u}_x$ at (50 m, 50 m, 0 m) computed with the DGSE method coupled with leap-frog scheme ($N = 2$, $\Delta t = 10^{-4}$) and the proposed space-time dG method ($N = r = 2$ and $\Delta t = 10^{-2}$ s). The results are compared with a reference semi-analytical solution obtained with the Thomson-Haskell propagation matrix method, [33]. Right: the time evolution of the error $e_x = |\boldsymbol{u}_{DG,x} - \boldsymbol{u}_{TH,x}|$.

Declaration of competing interest

The authors declare that they have no known competing financial interests or personal relationships that could have appeared to influence the work reported in this paper.

Acknowledgements

Paola F. Antonietti and Ilario Mazzieri have been partially supported by the SIR Research Grant no. RBSI14VTOS funded by MIUR – Italian Ministry of Education, Universities and Research. This work was partially supported by "National Group of Computing Science" (GNCS-INdAM).

Appendix A. Supplementary material

Supplementary material related to this article can be found online at https://doi.org/10.1016/j.jcp.2020.109685.

References

[1] D.S. Abdi, F.X. Giraldo, Efficient construction of unified continuous and discontinuous Galerkin formulations for the 3d Euler equations, J. Comput. Phys. 320 (2016) 46–68.
[2] C. Adam, D. Adam, F. Kopf, I. Paulmichl, Computational validation of static and dynamic plate load testing, Acta Geotech. 4 (4) (2009) 35–55.
[3] R.A. Adams, J.J.F. Fournier, Sobolev Spaces, second edition, Pure and Applied Mathematics, vol. 140, Elsevier, Amsterdam, 2003.

[4] S. Adjerid, H. Temimi, A discontinuous Galerkin method for the wave equation, Comput. Methods Appl. Mech. Eng. 200 (5) (2011) 837–849.
[5] P.F. Antonietti, B. Ayuso de Dios, I. Mazzieri, A. Quarteroni, Stability analysis of discontinuous Galerkin approximations to the elastodynamics problem, J. Sci. Comput. 68 (2016) 143–170.
[6] P.F. Antonietti, F. Bonaldi, I. Mazzieri, A high-order discontinuous Galerkin approach to the elasto-acoustic problem, Comput. Methods Appl. Mech. Eng. 358 (2020).
[7] P.F. Antonietti, A. Cangiani, J. Collis, Z. Dong, E. Georgoulis, S. Giani, P. Houston, Review of discontinuous Galerkin finite element methods for partial differential equations on complicated domains, in: Lecture Notes in Computational Science and Engineering, vol. 114, 2016, pp. 279–308.
[8] P.F. Antonietti, N. Dal Santo, I. Mazzieri, A. Quarteroni, A high-order discontinuous Galerkin approximation to ordinary differential equations with applications to elastodynamics, IMA J. Numer. Anal. 38 (4) (2018) 1709–1734.
[9] P.F. Antonietti, C. Facciolà, G. Pennesi, P. Houston, I. Mazzieri, M. Verani, High-order discontinuous Galerkin methods on polyhedral grids for geophysical applications: seismic wave propagation and fractured reservoir simulations, in: D. Di Pietro, L. Formaggia, R. Masson (Eds.), Polyhedral Methods in Geosciences, in: SEMA-SIMAI Springer Series, 2020, to appear.
[10] P.F. Antonietti, A. Ferroni, I. Mazzieri, R. Paolucci, A. Quarteroni, C. Smerzini, M. Stupazzini, Numerical modeling of seismic waves by discontinuous spectral element methods, ESAIM Proc. Surv. 61 (2018) 1–37.
[11] P.F. Antonietti, A. Ferroni, I. Mazzieri, A. Quarteroni, Dispersion-dissipation analysis of 3D continuous and discontinuous spectral element methods for the elastodynamics equation, Int. J. Geophys. 211 (3) (2017) 1554–1574.
[12] P.F. Antonietti, I. Mazzieri, High-order discontinuous Galerkin methods for the elastodynamics equation on polygonal and polyhedral meshes, Comput. Methods Appl. Mech. Eng. 342 (2018) 414–437.
[13] P.F. Antonietti, I. Mazzieri, A. Quarteroni, F. Rapetti, Non-conforming high order approximations of the elastodynamics equation, Comput. Methods Appl. Mech. Eng. 209 (2012) 212–238.
[14] C. Bajer, Triangular and tetrahedral space-time finite elements in vibration analysis, Int. J. Numer. Methods Eng. 23 (1986) 2031–2048.
[15] L. Banjai, E.H. Georgoulis, O. Lijoka, A Trefftz polynomial space-time discontinuous Galerkin method for the second order wave equation, SIAM J. Numer. Anal. 55 (1) (2017) 63–86.
[16] M. Behr, Simplex space–time meshes in finite element simulations, Int. J. Numer. Methods Fluids 57 (2008) 1421–1434.
[17] S.C. Brenner, Korn's inequalities for piecewise H^1 vector fields, Math. Comput. 73 (247) (2004) 1067–1087.
[18] A. Cangiani, Z. Dong, E.H. Georgoulis, P. Houston, *hp*-version discontinuous Galerkin methods for advection-diffusion-reaction problems on polytopic meshes, Modél. Math. Anal. Numér. 50 (2016) 699–725.
[19] A. Cangiani, E.H. Georgoulis, P. Houston, *hp*-version discontinuous Galerkin methods on polygonal and polyhedral meshes, Math. Models Methods Appl. Sci. 24 (10) (2014) 2009–2041.
[20] C. Canuto, M.Y. Hussaini, A. Quarteroni, T.A. Zang, Spectral Methods: Fundamentals in Single Domains, Springer, Berlin, 2006.
[21] C. Canuto, M.Y. Hussaini, A. Quarteroni, T.A. Zang, Spectral Methods: Evolution to Complex Geometries and Applications to Fluid Dynamics, 2007.
[22] M. Delfour, W. Hager, F. Trochu, Discontinuous Galerkin methods for ordinary differential equations, Math. Comput. 36 (154) (1981) 455–473.
[23] M. Dumbser, V. Casulli, A staggered semi-implicit spectral discontinuous Galerkin scheme for the shallow water equations, Appl. Math. Comput. 219 (15) (2013) 8057–8077.
[24] M. Dumbser, C.-D. Munz, ADER discontinuous Galerkin schemes for aeroacoustics, C. R., Méc. 333 (2003) 683–687.
[25] J. Erickson, D. Guoy, J. Sullivan, A. Üngör, Building space-time meshes over arbitrary spatial domains, Eng. Comput. 20 (2005) 342–353.
[26] J. Erickson, D. Guoy, J.M. Sullivan, A. Üngör, Building spacetime meshes over arbitrary spatial domains, Eng. Comput. 20 (4) (2005) 342–353.
[27] F. Fambri, M. Dumbser, Spectral semi-implicit and space–time discontinuous Galerkin methods for the incompressible Navier–Stokes equations on staggered Cartesian grids, Appl. Numer. Math. 110 (2016) 41–74.
[28] D.A. French, A space-time finite element method for the wave equation, Comput. Methods Appl. Mech. Eng. 107 (1) (1993) 145–157.
[29] D.A. French, T.E. Peterson, A continuous space-time finite element method for the wave equation, Math. Comput. 65 (1996) 491–506.
[30] E.H. Georgoulis, E. Hall, P. Houston, Discontinuous Galerkin methods for advection-diffusion-reaction problems on anisotropically refined meshes, SIAM J. Sci. Comput. 30 (1) (2007/08) 246–271.
[31] J. Gopalakrishnan, M. Hochsteger, J. Schöberl, C. Wintersteiger, An explicit mapped tent pitching scheme for Maxwell equations, arXiv preprint arXiv: 1906.11029, 2019.
[32] R. Griesmaier, P. Monk, Discretization of the wave equation using continuous elements in time and a hybridizable discontinuous Galerkin method in space, J. Sci. Comput. 58 (2) (2014) 472–498.
[33] N.A. Haskell, The dispersion of surface waves on multilayered media, Bull. Seismol. Soc. Am. 43 (1953) 17–43.
[34] T. Hughes, G. Hulbert, Space-time finite element methods for elastodynamics: formulation and error estimates, Comput. Methods Appl. Mech. Eng. 66 (1988) 339–363.
[35] T.J. Hughes, L.P. Franca, G.M. Hulbert, A new finite element formulation for computational fluid dynamics: VIII. The Galerkin/least-squares method for advective-diffusive equations, Comput. Methods Appl. Mech. Eng. 73 (2) (1989) 173–189.
[36] T.J. Hughes, G.M. Hulbert, Space-time finite element methods for second-order hyperbolic equations, Comput. Methods Appl. Mech. Eng. 84 (3) (1990) 327–348.
[37] A. Idesman, Solution of linear elastodynamics problems with space–time finite elements on structured and unstructured meshes, Comput. Methods Appl. Mech. Eng. 196 (2007) 1787–1815.
[38] C. Johnson, Discontinuous Galerkin finite element methods for second order hyperbolic problems, Comput. Methods Appl. Mech. Eng. 107 (1) (1993) 117–129.
[39] J. Kacur, Method of Rothe in evolution equations, in: Lecture Notes in Mathematics, vol. 1192, 1970, pp. 23–34.
[40] Z. Kamont, Numerical method of lines, in: Hyperbolic Functional Differential Inequalities and Applications, Springer, Netherlands, 1999, pp. 181–204.
[41] O. Karakashian, C. Makridakis, Convergence of a continuous Galerkin method with mesh modification for nonlinear wave equations, Math. Comput. 74 (2005) 85–102.
[42] U. Köcher, M. Bause, Variational space–time methods for the wave equation, J. Sci. Comput. 61 (2) (2014) 424–453.
[43] R. Kosloff, D. Kosloff, Absorbing boundaries for wave propagation problems, J. Comput. Phys. 63 (2) (1986) 363–376.
[44] A. Kroopnick, Bounded and L^2-solutions to a second order nonlinear differential equation with a square integrable forcing term, Int. J. Math. Math. Sci. 22 (3) (1999) 569–571.
[45] F. Lörcher, G. Gassner, C.-D. Munz, A discontinuous Galerkin scheme based on a space-time expansion. I. Inviscid compressible flow in one space dimension, J. Sci. Comput. 32 (2) (2007) 175–199.
[46] I. Mazzieri, M. Stupazzini, R. Guidotti, C. Smerzini, SPEED: spectral elements in elastodynamics with discontinuous Galerkin: a non-conforming approach for 3D multi-scale problems, Int. J. Numer. Methods Eng. 95 (12) (2013) 991–1010.
[47] N.C. Nguyen, J. Peraire, B. Cockburn, High-order implicit hybridizable discontinuous Galerkin methods for acoustics and elastodynamics, J. Comput. Phys. 230 (2011) 3695–3718.
[48] I. Perugia, D. Schötzau, An *hp*-analysis of the local discontinuous Galerkin method for diffusion problems, J. Sci. Comput. 17 (1–4) (2002) 561–571.
[49] I. Perugia, J. Schöberl, P. Stocker, C. Wintersteiger, Tent pitching and Trefftz-dg method for the acoustic wave equation, Comput. Math. Appl. (2020).

[50] B. Rivière, S. Shaw, M.F. Wheeler, J.R. Whiteman, Discontinuous Galerkin finite element methods for linear elasticity and quasistatic linear viscoelasticity, Numer. Math. 95 (2) (2003) 347–376.
[51] B. Rivière, S. Shaw, J. Whiteman, Discontinuous Galerkin finite element methods for dynamic linear solid viscoelasticity problems, Numer. Methods Partial Differ. Equ. 23 (5) (2007) 1149–1166.
[52] C. Schwab, *p*- and *hp*- Finite Element Methods: Theory and Applications in Solid and Fluid Mechanics, Oxford University Press, 1998.
[53] V. Sharma, K. Fujisawa, A. Murakami, Velocity-based time-discontinuous Galerkin space-time finite element method for elastodynamics, Soil Found. 58 (2018) 491–510.
[54] R. Stacey, Improved transparent boundary formulations for the elastic-wave equation, Bull. Seismol. Soc. Am. 78 (6) (1988) 2089–2097.
[55] M. Tavelli, M. Dumbser, A high order semi-implicit discontinuous Galerkin method for the two dimensional shallow water equations on staggered unstructured meshes, Appl. Math. Comput. 234 (2014) 623–644.
[56] M. Tavelli, M. Dumbser, Arbitrary high order accurate space-time discontinuous Galerkin finite element schemes on staggered unstructured meshes for linear elasticity, J. Comput. Phys. 366 (2018) 386–414.
[57] M.M. Tawfik, Y.M. El-Mossallamy, Application of the finite element method for investigating the dynamic plate loading test, Ain Shams Eng. J. 8 (1) (2017) 39–49.
[58] T. Tezduyar, S. Sathe, R. Keedy, K. Stein, Space–time finite element techniques for computation of fluid–structure interactions, Comput. Methods Appl. Mech. Eng. 195 (2006) 2002–2027.
[59] L.L. Thompson, P.M. Pinsky, A space-time finite element method for structural acoustics in infinite domains part 1: formulation, stability and convergence, Comput. Methods Appl. Mech. Eng. 132 (3) (1996) 195–227.
[60] E. Toro, V. Titarev, Solution of the generalized Riemann problem for advection–reaction equations, Proc. R. Soc. A 458 (2002) 271–281.
[61] E. Toro, V. Titarev, ADER schemes for three-dimensional non-linear hyperbolic systems, J. Comput. Phys. 204 (2005) 715–736.
[62] A. Üngör, A. Sheffer, Tent-pitcher: a meshing algorithm for space-time discontinuous Galerkin methods, in: Proceedings 9th International Meshing Roundtable, vol. 196, 2000, pp. 111–122.
[63] N.J. Walkington, Combined DG–CG time stepping for wave equations, SIAM J. Numer. Anal. 52 (2014) 1398–1417.
[64] Y. Yang, S. Chirputkar, D.N. Alpert, T. Eason, S. Spottswood, D. Qian, Enriched space–time finite element method: a new paradigm for multiscaling from elastodynamics to molecular dynamics, Int. J. Numer. Methods Eng. 92 (2) (2012) 115–140.